ABSTRACT

Title: STOCHASTIC ELECTRON TRAJECTORIES AND WAVE INTERACTION IN RELATIVISTIC GYRO-TRAVELING-WAVE AMPLIFIERS.

Roland Ngogang,
Master of Science, 2005

Directed By: Professor Victor L. Granatstein,
Department of Electrical Engineering

Gyro-traveling-wave amplifiers (gyro-TWAs) are types of gyrodevices, which take advantage of the cyclotron maser instability to produce coherent electromagnetic (EM) radiation from electrons gyrating in an external magnetic field and interacting with fast traveling waves. For high power applications, gyrodevices often require relativistic electron beams and operate at high cyclotron harmonics. In such conditions, if the EM wave is large enough, the electron cyclotron frequency can vary significantly in the process of interaction with the wave. This can lead to the overlapping of cyclotron resonances at different harmonics, which can cause electrons to exhibit stochastic trajectories.

In devices operating at cyclotron harmonics, it is possible for the electron beam to excite a wave at a given harmonic. This wave, in turn, can excite other waves at frequencies different from the operating frequency. The interaction between such

waves is a nonlinear effect. In relativistic gyrodevices, this wave interaction may be affected by the overlapping of cyclotron resonances. This thesis presents theoretical analysis of (a) the effect of overlapping of cyclotron resonances on electron trajectories (b) wave interaction in relativistic gyro-TWAs.

STOCHASTIC ELECTRON TRAJECTORIES AND WAVE INTERACTION IN RELATIVISTIC GYRO-TRAVELING-WAVE AMPLIFIERS.

By

Roland Ngogang.

Thesis submitted to the Faculty of the Graduate School of the
University of Maryland, College Park, in partial fulfillment
of the requirements for the degree of
Master of Science
2005

Advisory Committee:
Professor Victor L. Granatstein, Chair
Dr. Gregory S. Nusinovich
Professor Thomas M. Antonsen, Jr.

Acknowledgements

I would like to express my deepest gratitude to Prof. Victor Granatstein for giving me the opportunity to be part of the exciting gyrotron research at the University of Maryland. I am immensely grateful to Dr. Gregory Nusinovich whose patience and constant support were invaluable to my learning. I thank Professor Thomas Antonsen whose advices were useful for my research.

I would like to thank the IREAP staff especially Carol Bellamy, Nancy Boone, Dorothea Brosius, Janice Shoonever and Ed Condon for their prompt assistance with administrative and technical matters.

I am grateful to my friend and colleague Oleksandr Sinitsyn who helped me a great deal with my first numerical simulations. Together, we spent hours sometimes looking for errors in my codes. I also thank my former and current office mates: Steve Gouvea, Karthik Bharathan, Andrej Rasevic, Ioannis Stamatiou, Swati Tiwari, Pragya Purohit, and Netsanet Gebeyehu for the very friendly and comfortable working environment. Special mention is due to my colleague Todd Firestone for editing my thesis, and for being a good friend.

Finally, I am eternally grateful to my parents for their unconditional love and support, without it, I probably would have never made it to graduate school.

Table of Contents

List of Figures

Chapter 1: Introduction

1.1 Historical background

Microwaves are electromagnetic (EM) waves of frequency ranging from 1 GHz to 300 GHz (wavelength of 30 cm to 1 mm in free space). The origin of microwave sources can be traced back to the first demonstration of the existence of EM waves by Heinrich Hertz in 1887. His experiment proved that electrical signals could travel through open air as predicted more than two decades earlier by James Maxwell [1]. This discovery motivated research in radio communication and detection that led to the advent of the first useful microwave sources. These microwave sources were vacuum tubes in which RF power was derived from a DC electron beam traveling in a waveguide or resonator structure. The first microwave sources included the magnetron invented in 1921 by Albert Hall, the klystron invented by the Variant brothers in 1937 and the traveling wave tube (TWT) invented by Rudolph Kompfner in 1942 (see Refs. 2, 3 and 4 for a description of these devices).

The strong interest in high power microwave sources during World War II led to the development of very efficient high power magnetrons. Over a decade after the War, magnetrons remained the microwave source of choice for radar applications [3]. They were later replaced by the klystrons for these applications because the latter were found to have the advantage of delivering high pulse or continuous wave (CW) power with medium bandwidth and high gain. Advances in satellite communication and military radar systems research led to the development of wideband TWT amplifiers, which became widely used in civilian and military radar systems [3, 4].

While vacuum tubes remain the predominant source of high power microwaves they have become almost inexistent in the low power realm where advances in solid-state technology have rendered them obsolete. The small size of solid-state devices has made their production significantly cost-efficient compared to microwave tubes. Starting from the 1960s, it has also made it possible to integrate low power microwave systems on a single chip. These devices can be encountered in almost all applications affecting our daily life today. Some of these applications include TV and radio broadcast, long distance telephone, highway traffic monitoring and control, food preservation, automatic toll collection and microwave ovens [5].

Magnetrons, klystrons and traveling-wave tubes are still the most common types of vacuum tubes in use today for high-power applications in the frequency range 1-30 GHz. At higher frequencies, millimeter wave (30 to 300 GHz) and sub-millimeter wave (>300 GHz) ranges, other types of vacuum tubes called fast-wave devices have gained prominence, in particular gyrotrons. These devices are used in fusion experiments for electron cyclotron heating of confined plasmas, advanced radar systems, industrial processing. They can also be used in particle accelerators as well as medical imaging and various kinds of spectroscopy [3, 6-10]. In the next section we briefly describe the basic principle of vacuum tubes' operation.

1.2 Basic physics of microwave tubes

The basic operating principle of most microwave tubes consists of the conversion of the electron kinetic energy to coherent electromagnetic radiation. Electrons radiate electromagnetic energy in one of three ways depending on the type of microwave tube [9-11]: Cherenkov or Smith-Purcell radiation, transition radiation, and

bremsstrahlung radiation. In all three cases coherent radiation is only achieved after electrons have been bunched together.

Cherenkov radiation occurs when electrons travel in a medium with a velocity υ greater than the phase velocity ($\upsilon_{ph} = c/n$, where the medium refractive index n is greater than unity) of the EM waves present in the medium. These waves are called slow waves because their phase velocity is smaller than the speed of light ($\upsilon_{ph} < c$). Traveling-wave tubes and backward-wave oscillators (BWO's) are some examples of the microwave devices based on Cherenkov radiation. They are also known as Cherenkov devices.

Transition radiation occurs when electrons travel through a medium with a non-uniform index of refraction or experience some perturbation in the medium due to conducting grids or plates for example. Klystrons are some of the devices based on this principle.

When electrons oscillate in a constant magnetic or electric field with a variable velocity, the bremsstrahlung radiation occurs. Electrons radiate Doppler-shifted waves whose frequencies are close to harmonics of the frequency of the electron oscillations Ω:

$$\omega - k_z \upsilon_z \cong s\Omega . \tag{1.1}$$

Here $k_z \upsilon_z$ represents the Doppler-shift and s is the resonant harmonic number. The radiated waves can be either fast (i.e. $\upsilon_{ph} = \omega / k_z > c$) or slow (i.e. $\upsilon_{ph} < c$) since any wave phase velocity can satisfy (1.1). This is the basic principle behind cyclotron resonance masers (CRM's) and free electron lasers (FEL's).

In all these microwave sources electrons interact with the EM wave in a microwave circuit (waveguide or cavity) to form electron bunches. These bunches consist of electrons oscillating in phase. The electron beam bunching mechanism depends on the configuration of the interaction structure and the arrangement of the magnetic and electric fields. The radiated electromagnetic energy from electron bunches is absorbed by the electromagnetic wave, which grows in the process. The interaction between the beam and the wave in the microwave circuit is similar to the plasma-wave interaction, which can result in either of two types of instability: absolute instability or convective instability. The absolute instability can be used to form an oscillator while the convective instability can be used to achieve amplification [11-13].

High power microwave tubes can be classified in two major groups: fast wave devices and slow-wave devices. The slow-wave devices consist of a periodic slow-wave interaction structure (usually a rippled wall, helix, or disk-loaded waveguide). They include among others TWTs and BWOs. Because an electron beam travels along the axis of the structure in a straight line, these devices are also referred to as linear-beam devices. In these devices the electromagnetic waves propagate very close to the surface of the waveguide or cavity structure. Therefore, efficient interaction between the electron beam and the wave takes place when the distance between the beam and the surface of the waveguide or cavity structure is smaller than the wavelength. This gives rise to increased power loss due to wall heating, which leads to a net decrease of the output microwave power. As the wavelength shortens, the size of the interaction space gets smaller and this effect is more pronounced. The

fabrication of the device also becomes very difficult. The small size requirement has hindered the development of high-power linear-beam devices operating in the millimeter wave range. Indeed it has been shown that at very high frequencies the average radiated power and the operating frequency of these devices are related as follows: $Power \times frequency^2 = \text{constant}$ [10]. Therefore, the average microwave power drops significantly as the frequency increases.

Fast-wave devices offer two distinct advantages over slow-wave devices: the interaction circuit does not need to have periodic variation, i.e. a smooth-metal waveguide can be used, and the waves do not need to be localized near the waveguide walls [6,9,10]. Therefore, the interaction space can be extended in the transverse direction. The use of larger structures makes it possible for fast-wave devices to handle high power and operate at frequencies well above 100 GHz. Gyrotrons are the most prominent fast-wave devices that can operate at high levels of CW power at millimeter and sub-millimeter wavelengths. In the next section a brief description of the gyrotron is presented.

1.3 Gyrotrons

1.3.1 Principle of operation

Gyrotrons, also called cyclotron resonance masers or gyrodevices, are high power microwave sources of coherent millimeter or sub-millimeter radiation. They take advantage of the synchronism condition (1.1) and a fast-wave interaction structure to transfer energy from electrons gyrating in a strong constant magnetic field to an EM wave. Coherent radiation from electrons gyrating in a constant magnetic

field and interacting with fast EM waves was discovered in the late 1950s by three scientists working independently [8, 12]: R. Twiss in Australia, J. Schneider in the US and A. Gaponov in the USSR. Using a scheme based on the electron cyclotron maser (ECM) instability, Gaponov and his co-workers invented the gyrotron in 1967 [8].

In its simplest arrangement (shown in Figure 1.1), the gyrotron consists of a magnetron injection gun that produces an annular beam, an interaction region (a cavity) placed at the center of a strong magnet, and an RF extraction region. When a pulsed or continuous voltage is applied to the anode of the gun, an electric field is created at the cathode. In the region between the cathode and the anode the electric field is mostly perpendicular to the magnetic field generated by the solenoid. In this region, the electrons experience a constant drift velocity. As the electrons reach the end of the cathode-anode region, the electric field lines change from mostly perpendicular to parallel to the magnetic field lines. Therefore, the electrons acquire both orbital and axial velocity components. They gyrate helically about a fixed guiding center, where the radius of the path, the Larmor radius ($r_L = \upsilon_\perp / \Omega$), is small compared to the radius of the beam, so that the beam remains annular as it propagates. The electrons move toward the interaction region through a growing magnetic field. The electron orbital momentum increases due to adiabatic compression: $p_\perp^2 / B = const$. In the interaction region the magnetic field is uniform. Here electrons interact with the transverse electric (TE) eigen mode of the cavity and transform a part of their kinetic energy into microwave energy. Then, the spent beam leaves the cavity through an up-taper to be collected on a uniform waveguide wall.

The generated microwave power is extracted axially through the output window (shown on the right) into a waveguide to be used. In the case of radial extraction the microwave power is converted into a Gaussian beam with the use of a built-in mode converter before extraction through the window. For efficient coupling to the wave, electrons must have a significant transverse velocity component because energy transfer occurs as a result of the interaction between the transverse velocity component of the gyrating electrons and the TE modes (RF fields) of the cavity structure. The physical description of the interaction between the electron beam and the wave is given in the next section.

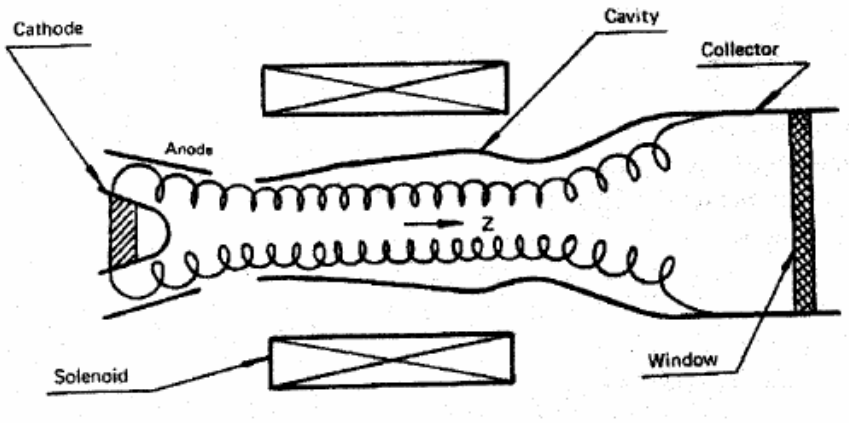

Figure 1.1: Simplified gyrotron arrangement [8].

1.3.2 ECM instability

The electron cyclotron maser instability is the mechanism responsible for the energy transfer from the electron beam to the EM wave in gyrodevices. It originates from the relativistic dependence of electron cyclotron frequency on energy [8, 15]:

$$\Omega = \frac{eB_0}{mc\gamma}, \tag{1.2}$$

where e is the electron charge, B_0 is the constant magnetic field applied on electrons, m is the electron rest mass, and γ is the relativistic factor ($\gamma = 1 + eV_b / mc^2$, here eV_b is the electron kinetic energy and mc^2 is the electron rest energy).

Consider the beam of electrons uniformly distributed in phase at the entrance of the interaction region as shown in Figure 1.2 (a). When this beam encounters the transverse field of the cavity (or waveguide) as it begins to move through the interaction space, electrons experience a force that causes some of them to accelerate (electrons 2, 3 and 4) and others to decelerate (electrons 6, 7, 8) or remain undisturbed (electrons 1 and 5). An electron is accelerated (gains energy), if its transverse velocity is in a direction opposite to that of the electric field. If the transverse velocity of an electron is in the same direction as the electric field, this electron is decelerated instead (it looses energy). Figure 1.2 (a) illustrates this modulation of electrons with a plot of the final electron phase distribution shown in a solid circle. Since the electron cyclotron frequency is inversely proportional to the electron energy, accelerated electrons fall behind in phase while decelerated electrons lead in phase. Therefore, a phase bunching of the electron beam occurs as shown in Figure 1.2 (b). It is important to note that if the RF field is turned off after the initial electron energy modulation the phase bunching of electrons may continue. This characteristic of the bunching mechanism in gyrotrons is used extensively to obtain tight bunches in these devices (especially in gyroklystrons and gyrotwystrons). Energy is extracted from the bunched electrons if the frequency of the oscillating electric field is slightly greater than the cyclotron frequency, so that the electron

bunch is situated in the decelerating phase of the electric field as shown in Figure 1.2 (c). The RF field may experience a substantial growth in amplitude in the process. If the interaction is allowed to continue for too long time, the bunched particles eventually start to gain energy and the field amplitude will decrease.

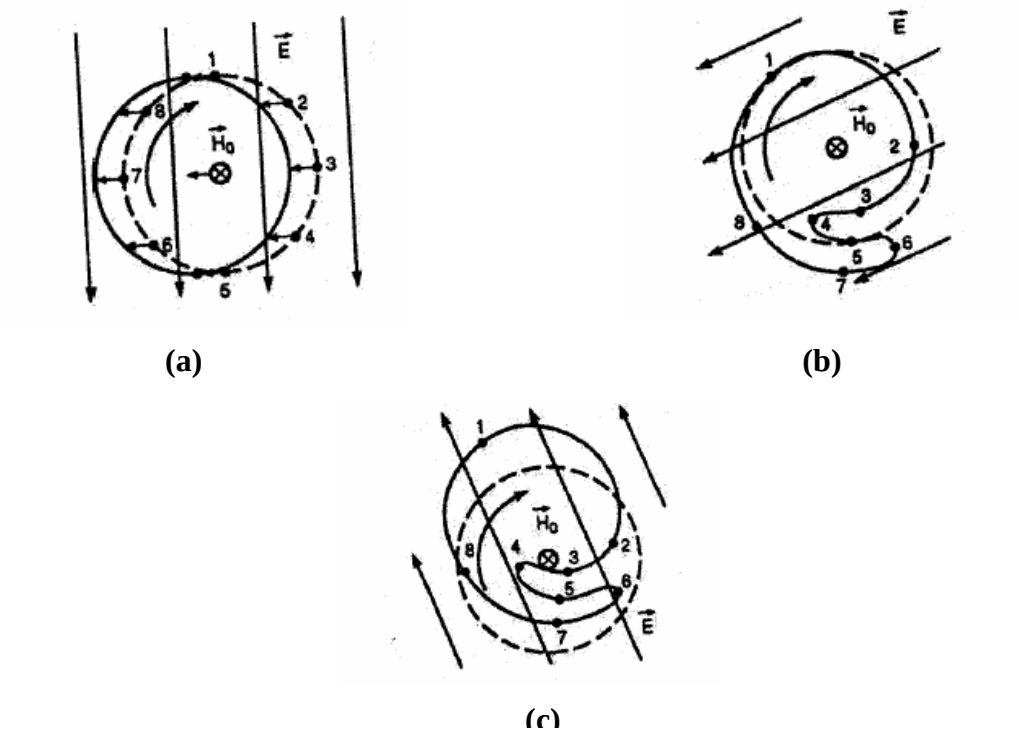

Figure 1.2: Illustration of the bunching mechanism in the gyrotron. (a) Electrons with uniform phase distribution initially are modulated by a circularly polarized RF electric field. (b) Electrons experience phase bunching due to the initial modulation. (c) The electron bunch is decelerated if the phase of the RF field has a frequency slightly higher than the cyclotron frequency [8].

It follows from (1.1) that electrons stay in resonance with the wave in the process of phase bunching when the electron cyclotron resonance mismatch (phase difference between the electron gyrophase and the phase of the wave) does not exceed 2π . That is

$$\left|\omega - s\Omega\right| T \le 2\pi \,, \tag{1.3}$$

where $T = \upsilon_z / L$ is the electron transit time through the interaction space of length L. In (1.3) the Doppler term is ignored because it is small in gyrotrons operating near cutoff frequency. From (1.2) one can find that when the electron energy changes by a small amount $\Delta\gamma$ the cyclotron frequency changes by an amount $\Delta\Omega$:

$$\frac{\Delta\Omega}{\Omega_0} = -\frac{\Delta\gamma}{\gamma_0} \,. \tag{1.4}$$

Here Ω_0 and γ_0 are the initial electron cyclotron frequency and energy, respectively. The change in cyclotron frequency leads to a shift in the cyclotron resonance mismatch, which has to fulfill condition (1.3)

$$s\Delta\Omega T = s\frac{\Delta\gamma}{\gamma_0}\Omega_0 T \le 2\pi \,. \tag{1.5}$$

If we assume all of the kinetic energy of the electrons is transferred to the EM wave, then the operating voltage can be related to the number of electron orbits, $N = \Omega_0 T / 2\pi$, in the interaction space as follows:

$$\frac{\Delta\gamma}{\gamma_0} = \frac{eV_b}{mc^2\gamma_0} \le \frac{1}{sN} \,. \tag{1.6}$$

Therefore, if the beam is weakly relativistic (i.e., $eV_b \ll mc^2$), a large number of electron orbits is required for the efficient phase bunching and deceleration of electrons. The resonant interaction has a narrow bandwidth making it possible to use an RF field of moderate amplitude. However if the beam is made up of relativistic electrons, condition (1.6) holds for $N \sim 1$. Large field amplitudes are required, which may cause RF breakdown and greatly broaden the cyclotron resonance band. In the

case of a large resonance band, several modes may be excited simultaneously, thus leading to reduced interaction efficiency with the desired mode.

The bunching mechanism and subsequent transfer of energy to the wave described above corresponds to the interaction between the beam and the wave at the fundamental cyclotron resonance. A similar interaction is also possible at harmonics of the cyclotron frequency. In this case the electric field varies across the Larmor radius of gyrating electrons. In general, for interaction at the s^{th} cyclotron harmonic, the orbiting electrons experience a multipole electric field of order 2s [8,15]. The field structure for the first three cyclotron harmonics is shown in Figure. 1.3. In this case s electron bunches may be formed in the process of interaction at s^{th} cyclotron harmonic. Although operation at higher harmonics eliminates the need for large magnetic field, it requires stronger electric field for efficient interaction between the beam and the wave. Weak coupling between the beam and the wave at the desired high cyclotron harmonic can result in competition with modes operating at lower harmonics.

If the electron beam is relativistic, it is possible that the overlapping of cyclotron resonances at different cyclotron harmonics due to the widening of the resonance bands and an increasing RF field amplitude occurs. Figure 1.4 illustrates such an interaction in a second harmonic gyrotron. The possibility of overlapping of resonances at the first three cyclotron harmonics is illustrated there. In this figure the phase space corresponding to the fundamental harmonic moves to the right while the one corresponding to the third harmonic moves to the left in the reference frame of the second harmonic interaction. Therefore an electron bunch starting outside the

second harmonic resonance band can be accelerated by the third harmonic as shown by the dotted line [16].

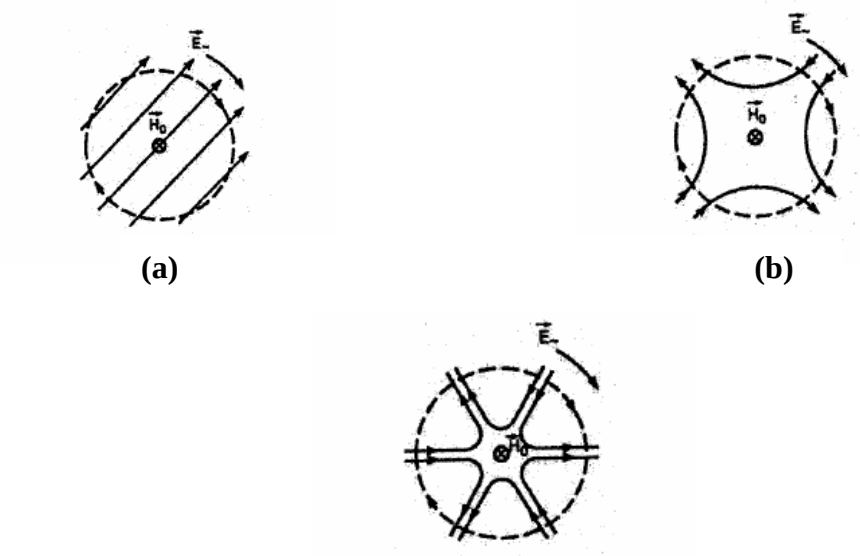

Figure 1.3: Transverse structure of the RF field for the case of resonance interaction at the first three cyclotron harmonics. (a) $s=1$ **(b)** $s=2$ **(c)** $s=3$ **[8].**

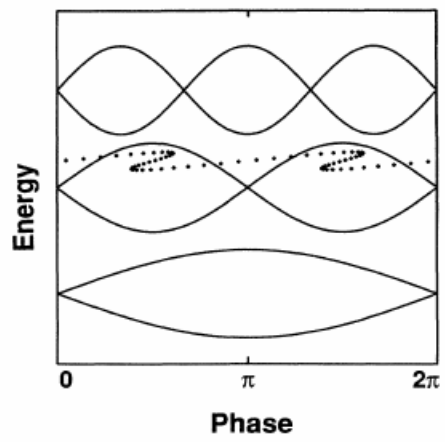

Figure 1.4: Illustration of the possible additional interaction at the first and third harmonics in a second harmonic relativistic gyrotron. The dotted line represents the second harmonic resonance interaction of an electron bunch with the field being disturbed by the third harmonic. Similar effect can occur with the fundamental harmonic if the field amplitude is large enough so that the distance between the first and second resonance bands is reduced [16].

1.3.3 Types of gyrotrons

Gyrotrons can be divided into two groups: gyrotron oscillators and gyrotron amplifiers. Oscillators have an internal or external feedback mechanism [11, 12]. To understand how coherent radiation is produced in a gyrotron oscillator it is important to recall that gyrating electrons traveling through a fast wave structure emit spontaneous radiation. This radiation can be associated with a wide frequency spectrum noise due to the discreteness nature of electrons charge. The eigen modes of the structure with frequencies that match up some of the spectrum frequencies will experience amplitude growth due to the feedback mechanism. If any of these modes is dominant (i.e., grows faster) it will interact strongly with the electron beam to form an electron bunch and coherent microwave radiation will be produced at this mode frequency.

Gyrotron amplifiers have no feedback mechanism [11, 12]. In this case a small input signal is fed into the interaction space. This signal frequency corresponds to that of an eigen mode of the interaction structure. In the process of interaction with the gyrating electrons, the EM field at the signal frequency (or its harmonics) grows. along the device axis. Therefore, in the case of an amplifier the amplitude and phase of the microwave radiation can be controlled.

Gyrotron oscillators are primarily used for plasma heating and current drive experiment in magnetic fusion research. They include the single cavity gyrotron oscillator, also called gyromonotron, and the gyrotron backward-wave oscillator (gyro-BWO), which can be frequency tunable.

Gyrotron amplifiers include gyroklystrons, gyro-traveling-wave-tubes (gyro-TWTs), and gyrotwystrons. The gyroklystron consists of an input cavity, one or more intermediate cavities, and an output cavity. Field free drift sections separate the cavities. Coherent microwave radiation is generated through the interaction between the electron beam and standing waves. The gyroklystron is inherently a high output power device with a rather narrow bandwidth [8,12]. The gyrotwystron is essentially a gyroklystron with a traveling-wave output. For this reason it combines the merits of the gyroklystron (high gain) and the gyro-TWT (wide bandwidth).

1.3.4 Gyro-traveling-wave amplifiers (Gyro-TWAs)

Gyro-TWAs include the gyro-TWT and the gyrotwystron. These devices have a broad instantaneous bandwidth due to the use of a traveling-wave tube for energy extraction [12]. This characteristic, which makes gyro-TWAs suitable for radar applications, has motivated the development of high power gyro-TWAs operating at very high frequencies (see [6, 9, 12, and 17] for a discussion of some of the gyro-TWA experiments). Although most devices under development use moderate energetic beams, the successful testing of a gyro-TWT driven by a relativistic beam at the NRL in 1991 [6, 9] proved relativistic gyro-TWAs could be good candidate for driving linear accelerators or advanced millimeter-wave radars. The NRL gyro-TWT achieved 20MW at 35 GHz with 11% efficiency using an electron beam of 900 keV and 300 A [9]. Another noteworthy experiment to mention here is the MIT's 140 GHz gyro-TWT, which promises to deliver high average power at short millimeter wavelengths.

1.4 Motivations and outline

High power gyro-traveling-wave amplifiers considered for applications in the millimeter-wavelength range use relativistic electron beams [6, 7]. As mentioned above, the relativistic dependence of the electron cyclotron frequency can lead to a widening of the resonance band if the RF field amplitude is very large. Therefore, it is possible for electrons to interact with the RF field of a given wave at several cyclotron harmonics simultaneously. It means that in a second harmonic gyro-amplifier, for example, it is possible to have additional resonance interaction at the first and third harmonics, as shown in Figure 1.4 above.

This overlapping of resonances may cause electrons to exhibit stochastic trajectories. It is important that the beam be relativistic for this effect to occur because earlier studies in weakly relativistic gyrodevices operating at the fundamental harmonic did not find any sign of stochasticity in electron trajectories [18, 19]. Understanding chaos-like processes in relativistic gyro-amplifiers is important as they might lead to undesirable effects such as reduction of the net efficiency of the device or broadening of the radiation linewidth. This is particularly a concern for RF drivers in applications such as millimeter-wave radars and linear accelerators where precise phase control and low phase noise are very important [20].

When an RF driver excites a waveguide mode it is possible that this mode, in turn, excite other waveguide modes at harmonics of the signal frequency through nonlinear interaction with the relativistic electron beam. Mode interaction has been extensively studied in gyro-oscillators and shown to affect the efficient operation of

these devices [21-23]. In gyro-traveling amplifiers, the study of mode interaction has focused on the possible excitation of backward waves. However in these gyro-amplifiers, the nonlinear excitation of forward waves at harmonic frequencies of the operating frequency can result in the significant growth of undesired waves. The additional possibility of the overlapping of cyclotron resonances can enhance or suppress the effect of the nonlinear wave interaction on the output radiation. This thesis seeks to investigate such effect on the performance of relativistic gyro-TWAs.

The thesis is organized as follows: in Chapter 2, the equations describing the overlapping of cyclotron resonances in a second harmonic gyro-TWA are derived. Equations describing interaction between three waveguide modes interacting with an electron beam at the fundamental, second and third harmonics, respectively, are also presented in the same Chapter. The simulation results showing the effect of resonances overlap on electron trajectories are presented and analyzed in Chapter 3. In Chapter 4, the nonlinear interaction between three waveguide modes in relativistic gyro-TWAs is studied. The effect of the overlapping of cyclotron resonances on this interaction is discussed in the same Chapter. Some concluding remarks on the entire analysis are given in Chapter 5.

Chapter 2: General Formalism

2.1 Introduction

The theory presented follows from the nonlinear theory of interaction at arbitrary cyclotron harmonics between electrons moving periodically with a constant axial velocity and an electromagnetic wave first developed by Yulpatov [24] and later generalized by Nusinovich and Li in [25] for gyro-TWAs driven by a relativistic beam. Here second harmonic gyro-traveling-wave amplifiers are considered. The model consists of an ideal beam of relativistic electrons (velocity spread is not taken into account) gyrating in a constant magnetic field and interacting with traveling fast EM waves in a cylindrical structure. The theory accounts for the possibility of simultaneous interaction between the electrons and the EM waves at the first and third cyclotron harmonics as in Refs.16 and 26. The electromagnetic field has the temporal and spatial dependence of a wave when the beam is absent in the structure.

The chapter begins with a brief description of the dispersion diagram illustrating the interaction between the electron beam and the waveguide modes. Then a derivation of the self-consistent equations describing this interaction follows. Similar equations for the case of interaction between three waveguide modes and the electron beam are also presented.

2.2 Dispersion diagram

The dispersion diagram illustrates the interaction between the waves and the electron beam. In order to better explain this interaction it is expedient to derive the transverse field components of a cylindrical waveguide.

Let's assume the following representation for the electric and magnetic fields in a waveguide of length L:

$$\vec{E} = \Re e\left\{ A(z,t)\vec{E}_s(r_\perp)e^{i(\omega t - k_z z)} \right\} \tag{2.1}$$

$$\vec{H} = \Re e\left\{ A(z,t)\vec{H}_s(r_\perp)e^{i(\omega t - k_z z)} \right\}, \tag{2.2}$$

where $\vec{E}_s$ and $\vec{H}_s$ describe the transverse structure of the fields in the waveguide, $A(z,t)$ is the amplitude of the electromagnetic field, which varies slowly in both time and space. The variable $r_\perp$ represents the transverse coordinate (r,φ), k_z is the axial wavenumber. The fields $\vec{E}_s$ and $\vec{H}_s$ obey the following Maxwell's equations for waves with frequency ω and wavenumber $k = \omega/c$ in the source-free waveguide:

$$\nabla \times \vec{E}_s = -\frac{i\omega}{c}\vec{H}_s \tag{2.3}$$

$$\nabla \times \vec{H}_s = \frac{i\omega}{c}\vec{E}_s . \tag{2.4}$$

Here we assume that the dielectric and magnetic permeability constants are both equal to unity: $\varepsilon = \mu = 1$. Taking the curl of Eq. 2.4 and substituting it into the curl of Eq. 2.3 one can obtain the following wave equation,

$$\nabla^2 \vec{H}_s + \frac{\omega^2}{c^2}\vec{H}_s = 0 . \tag{2.5}$$

For TE modes, $\vec{H}_z = \vec{H}_s(r,\varphi)e^{-ik_z z}$ is a solution of the wave equation and $\vec{E}_z = 0$. The other EM field components can be written in terms of $\vec{H}_z$ through the Maxwell's equations as follows:

$$\vec{H}_r = -\frac{ik_z}{k_\perp^2}\frac{\partial H_z}{\partial r}\hat{r} \tag{2.6}$$

$$\vec{E}_\varphi = \frac{ik}{k_\perp^2}\frac{\partial H_z}{\partial r}\hat{\varphi} \tag{2.7}$$

$$\vec{H}_\varphi = -\frac{ik_z}{k_\perp^2 r}\frac{\partial H_z}{\partial \varphi}\hat{\varphi} \tag{2.8}$$

$$\vec{E}_r = -\frac{ik}{k_\perp^2 r}\frac{\partial H_z}{\partial \varphi}\hat{r}\,, \tag{2.9}$$

where $k_\perp^2 = \omega^2/c^2 - k_z^2$. Expressing the wave equation as a function of H_z in cylindrical coordinates, it becomes

$$\left(\frac{\partial^2}{\partial r^2} + \frac{1}{r}\frac{\partial}{\partial r} + \frac{1}{r^2}\frac{\partial^2}{\partial \varphi^2} + k_\perp^2\right)\vec{H}_z = 0\,. \tag{2.10}$$

A solution of this equation can be derived using the method of separation of variables [27]. If we assume $H_s(r_\perp) = R(r)P(\varphi)$ and substitute into Eq. 2.10 we obtain

$$\frac{r^2}{R}\frac{d^2R}{dr^2} + \frac{r}{R}\frac{dR}{dr} + r^2 k_\perp = -\frac{1}{P}\frac{d^2P}{d\varphi^2}\ . \tag{2.11}$$

Since each side of this equation depends only on a single variable, one can equate them to a constant and obtain the following

$$-\frac{1}{P}\frac{d^2P}{d\varphi^2} = k_\varphi^2\,, \tag{2.12}$$

$$r^2\frac{d^2R}{dr^2} + r\frac{dR}{dr} + (r^2k_\perp^2 - k_\varphi^2)R = 0\,. \tag{2.13}$$

The general solution to (2.12) is of the form

$$P(\varphi) = Ae^{\pm im\varphi}, \tag{2.14}$$

where *A* is a constant and m replaces k_φ, which must be an integer to ensure that H_z is periodic in φ. Equation 2.13 becomes

$$r^2 \frac{d^2R}{dr^2} + r\frac{dR}{dr} + (r^2k_\perp^2 - m^2)R = 0, \tag{2.15}$$

which has the form of a Bessel's differential equation. The general solution to this equation can be expressed as

$$R(r) = BJ_m(k_\perp r) + CY_m(k_\perp r). \tag{2.16}$$

Since the second order Bessel function $Y_m(k_\perp r)$ goes to infinity at $r = 0$, this term is not acceptable for our cylindrical waveguide. So, $H_s(r_\perp)$ can be written as

$$H_s(r_\perp) = J_m(k_\perp r)e^{\pm im\varphi}, \tag{2.17}$$

where the product of the two constants *A* and *B* has been set to unity. In order to define the perpendicular wavenumber $k_\perp$, it is important to recall the boundary condition in this case: the tangential component of the electric field at the waveguide wall must be equal to zero. Since $E_z = 0$, we must have $E_\varphi(r_\perp) = 0$ at $r = R_w$, where R_W is the radius of the waveguide. From Eqs. 2.7 and 2.17 we have

$$E_\varphi(r_\perp, z) = \frac{ik}{k_\perp} J'_m(k_\perp r)e^{-i(k_z z \pm m\varphi)}. \tag{2.18}$$

In order for E_φ to vanish at $r = R_w$ we must have

$$J'_m(k_\perp R_w) = 0. \tag{2.19}$$

If ν_{mp} represent the roots of $J'_m(x)$, that is $J'_m(\nu_{mp}) = 0$, where ν_{mp} is the *p-th* root of J'_m, then $k_\perp$ must have the value

$$k_{\perp} = \frac{\nu_{mp}}{R_w}. \tag{2.20}$$

The TE_{mp} modes that can propagate in a given cylindrical waveguide are determined by the perpendicular wavenumber defined in (2.20), where *m* refers to the number of angular (φ) variations and *p* refers to the number of radial (r) variations. Therefore, $k_{\perp}$ is a function of the waveguide cutoff frequency. The other transverse field components can be obtained in the same manner as E_{φ}. From equations 2.6, 2.8, 2.9, and 2.17 we have

$$\vec{H}_r = -\frac{ik_z}{k_{\perp}} J'_m(k_{\perp} r) e^{-i(k_z z \pm m\varphi)} \hat{r} \tag{2.21}$$

$$\vec{H}_{\varphi} = \pm \frac{k_z}{k_{\perp}^2} \frac{im}{r} J_m(k_{\perp} r) e^{-i(k_z z \pm m\varphi)} \hat{\varphi} \tag{2.22}$$

$$\vec{E}_r = \pm \frac{k}{k_{\perp}^2} \frac{im}{r} J_m(k_{\perp} r) e^{-i(k_z z \pm m\varphi)} \hat{r}. \tag{2.23}$$

From the wave equation it follows that

$$\omega^2 = c^2 (k_{\perp}^2 + k_z^2). \tag{2.24}$$

To simplify our treatment we assume that the axial wavenumber satisfies the following conditions:

$$\pi / L \ll k_z \ll \omega / c. \tag{2.25}$$

Here the first condition $(k_z \gg \pi / L)$ allows us to ignore the interaction with possible backward waves because it makes them nonresonant with electrons. The second condition $(k_z \ll \omega / c)$ allows us to neglect changes in the electron axial momentum.

As it was mentioned in Section 1.3.2 above, the transfer of energy from gyrating electrons to the EM wave occurs when the resonance condition (1.1):

$\omega - k_z \upsilon_z = s\Omega$ is verified. By plotting the dependence of the wave frequency on the axial wavenumber using both Eqs. 1.1 and 2.24 as shown in Figure 2.1 we obtain a dispersion diagram in the waveguide. Since equation 2.24 does not account for the coupling of the wave with the beam, this dispersion diagram is said to be uncoupled. Here the three straight dashed lines represent the beam lines at the first, second and third cyclotron harmonics. The point of efficient interaction between the beam and the wave is located where the beam line grazes the waveguide mode curves.

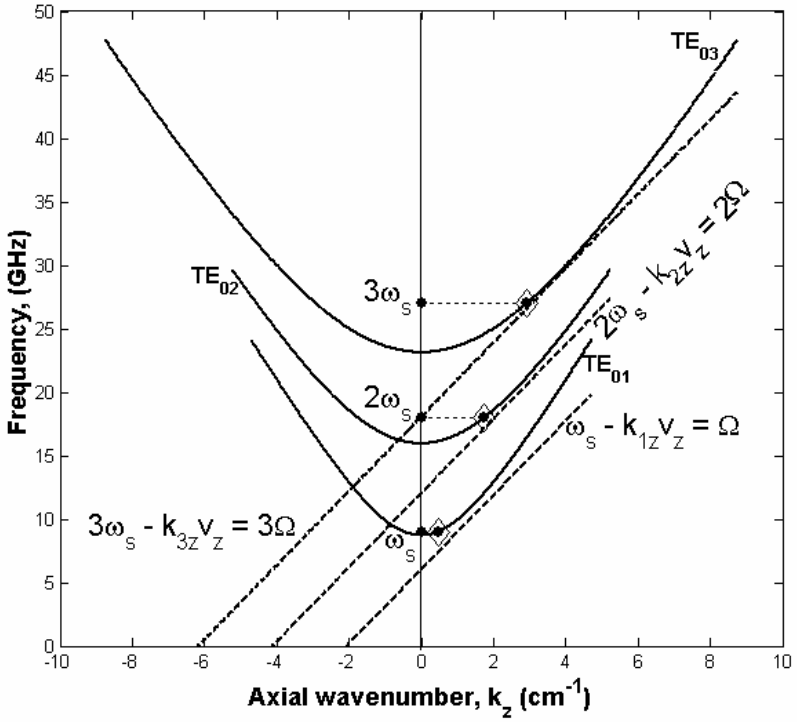

Figure 2.1: Uncoupled dispersion diagram showing the interaction between waveguide modes and the electron beam line at different harmonics.

2.3 Self-consistent equations for gyro-TWTs with overlapping cyclotron resonances

2.3.1 Field excitation equation

The derivation of field excitation presented here closely follows the theory in [22] and [23] with the exception that the field amplitude depends both on time and the axial length. We begin by substituting the electromagnetic field expressions (2.1) and (2.2) into the following Maxwell's equations

$$\nabla \times \vec{E} = -\frac{1}{c}\frac{\partial \vec{H}}{\partial t} \tag{2.26}$$

$$\nabla \times \vec{H} = \frac{1}{c}\frac{\partial \vec{E}}{\partial t} + \frac{4\pi}{c}\vec{j}\,. \tag{2.27}$$

to obtain

$$\left(\nabla_{\perp}^2 + \frac{\partial^2}{\partial z^2}\right)\vec{E} = \frac{1}{c^2}\frac{\partial^2 \vec{E}}{\partial t^2} + \frac{4\pi}{c^2}\frac{\partial \vec{j}}{\partial t}\,. \tag{2.28}$$

Here the beam current density is represented as

$$\vec{j} = \Re e\left\{\vec{j}_{\omega}\exp(i\omega t)\right\}. \tag{2.29}$$

Expanding both sides of (2.28) we have

$$\left(\nabla_{\perp}^2 + k_{\perp}^2\right)A\vec{E}_s + \vec{E}_s\left(\frac{\partial^2 A}{\partial z^2} - \frac{1}{c^2}\frac{\partial^2 A}{\partial t^2}\right) - 2i\left(k_z\frac{\partial A}{\partial z} - \frac{\omega}{c^2}\frac{\partial A}{\partial t}\right)\vec{E}_s = \frac{i\omega 4\pi}{c^2}\vec{j}_{\omega}\,. \tag{2.30}$$

Since the transverse field $\vec{E}_s$ obeys the homogeneous wave equation (2.5), and the field amplitude $A(z,t)$ is a slowly varying function of time ($\left|dA/dt\right| \ll \omega A$) and axial distance, one can reduce (2.30) to

$$\left(\frac{\partial A}{\partial z}+\frac{1}{\upsilon_{gr}}\frac{\partial A}{\partial t}\right)\vec{E}_s=-\frac{2\pi\omega}{c^2k_z}\vec{j}_\omega, \tag{2.31}$$

where υ_{gr} is the wave group velocity ($\upsilon_{gr}=c^2/\upsilon_{ph}=\frac{c^2}{\omega/k_z}$). Equation 2.31 is then dotted with $\vec{E}_s^*$ and integrated over the cross section area of the waveguide. It becomes

$$\left(\frac{\partial A}{\partial z}+\frac{1}{\upsilon_{gr}}\frac{\partial A}{\partial t}\right)E_s=-\frac{\omega}{2ck_zN_s}\int_{S_\perp}\vec{j}_{\omega\perp}\cdot\vec{E}_s^*e^{ik_zz}dS_\perp, \tag{2.32}$$

where N_s is the norm of the wave given by

$$N_s=\frac{c}{4\pi}\int_{s_\perp}\left|\vec{E}_s\right|^2ds_\perp. \tag{2.33}$$

Averaging (2.32) over the wave period and replacing the current density $\vec{j}_\omega$ by its inverse Fourier transform, equation 2.32 becomes

$$\frac{\partial A}{\partial z}+\frac{1}{\upsilon_{gr}}\frac{\partial A}{\partial t}=\frac{-1}{hN}\left\langle\int_{s_\perp}\left[\frac{1}{2\pi}\int_0^{2\pi}\vec{j}_\perp\cdot\vec{E}_s^*e^{-i(\omega t-k_zz)}d\left(\omega t_0\right)\right]ds_\perp\right\rangle, \tag{2.34}$$

where $h=k_z/k$ is the normalized axial wave number. Here we recall the charge conservation law

$$\rho dt=\frac{\rho\upsilon_{z0}}{\upsilon_z}dt_0=\frac{j_0}{\upsilon_z}dt_0, \tag{2.35}$$

which is applied to (2.34) to give

$$\frac{\partial A}{\partial z}+\frac{1}{\upsilon_{gr}}\frac{\partial A}{\partial t}=\frac{-1}{hN}\left\langle\int_{s_\perp}j_0\left[\frac{1}{2\pi}\int_0^{2\pi}\frac{\vec{\upsilon}_\perp\cdot\vec{E}_s^*}{\upsilon_{z0}}e^{-i(\omega t-k_zz)}d\left(\omega t_0\right)\right]ds_\perp\right\rangle. \tag{2.36}$$

This wave excitation equation will be revisited after we derive the equations of electron motion.

2.3.2 Electron motion equations

Motion of an electron in a guiding magnetic field and interacting with a TE wave can be represented by the Lorentz force equation

$$\frac{d\vec{p}}{dt} = -e\left\{\vec{E} + \frac{1}{c}\left[\vec{\upsilon} \times \left(\vec{H}_0 + \vec{H}\right)\right]\right\} \tag{2.37}$$

where $\vec{p}$ is the electron momentum, $\vec{\upsilon}$ is the electron velocity, $\vec{H}_0$ is the external magnetic field, $\vec{E}$ and $\vec{H}$ are the wave electric and magnetic fields, respectively. Introduce the following normalized parameters:

$$z' = \omega z / c\,, \tag{2.38}$$

$$\vec{p}' = \vec{p} / m_0 c\,, \tag{2.39}$$

$$A' = eA / m_0 c\omega\,, \tag{2.40}$$

$$\mu = eH_0 / m_0 c\omega = \Omega_0 / \omega\,, \tag{2.41}$$

$$\beta_z = \upsilon_z / c\,, \tag{2.42}$$

$$\beta_\perp = \upsilon_\perp / c\,, \tag{2.43}$$

Then, the Lorentz force equation can be rewritten as

$$\frac{d\vec{p}'}{dz'} + \mu\left(\frac{\vec{p}'}{p_z'} \times \hat{z}'\right) = -\frac{1}{\beta_z}\Re e\left\{A' e^{i(\omega t - k_z z)}\left[\vec{E}_s + \left(\vec{\beta} \times \vec{H}_s\right)\right]\right\} \tag{2.44}$$

$$= -\frac{1}{\beta_z}\Re e\left\{A' e^{i(\omega t - k_z z)}\vec{G}\right\},$$

where

$$\vec{G} = \vec{E}_s + \left(\vec{\beta} \times \vec{H}_s\right) \tag{2.45}$$

Assuming that the EM field amplitude is weaker than the external magnetic field, the transverse momentum and the position of the gyrating electrons can be represented as shown in Figure 2.2. Using normalized variables we have

$$p'_x = -p'_\perp \sin\theta\,, \qquad p'_y = p'_\perp \cos\theta\,, \tag{2.46}$$

$$x' = X' + r'_L \cos\theta\,, \qquad y' = Y' + r'_L \sin\theta\,, \tag{2.47}$$

where

$$\theta = \Omega\tau + \phi, \qquad t = t_0 + \tau\,. \tag{2.48}$$

$$X' = \omega X / c\,, \qquad Y' = \omega Y / c\,, \qquad r'_L = \omega r_L / c\,. \tag{2.49}$$

The parameters r'_L, X' and Y' represent the normalized Larmor radius and guiding center coordinates of the gyrating electrons, respectively. These parameters, as well as $p'_\perp$ and ϕ, are constant when the RF field is absent. In the presence of the RF field, due to the smallness of its amplitude in comparison with the external magnetic field, these parameters can be considered as slowly varying function during one period of gyration [8]. Therefore, from (2.44) to (2.47) one can obtain

$$\dot{p}'_\perp \sin\theta + p'_\perp \dot{\phi} \cos\theta = \frac{1}{\beta_z} \Re e\left\{ A' e^{i(\omega t - k_z z)} G_x \right\} \tag{2.50}$$

$$\dot{p}'_\perp \cos\theta - p'_\perp \dot{\phi} \sin\theta = -\frac{1}{\beta_z} \Re e\left\{ A' e^{i(\omega t - k_z z)} G_y \right\} \tag{2.51}$$

$$\dot{X}' + \dot{r}'_L \cos\theta - r'_L \dot{\psi} \sin\theta = 0 \tag{2.52}$$

$$\dot{Y}' + \dot{r}'_L \sin\theta - r'_L \dot{\psi} \cos\theta = 0 \tag{2.53}$$

$$\theta = \mu \int_0^z \frac{1}{p'_z} dz' + \phi \tag{2.54}$$

where the dots are used to indicate derivatives with respect to the normalized axial distance (d / dz'). The RF Lorentz force components G_x and G_y can be replaced by their polar coordinate representation given by

$$G_r = G_x \cos\theta + G_y \sin\theta, \tag{2.55}$$

$$G_\theta = -G_x \sin\theta + G_y \cos\theta \tag{2.56}$$

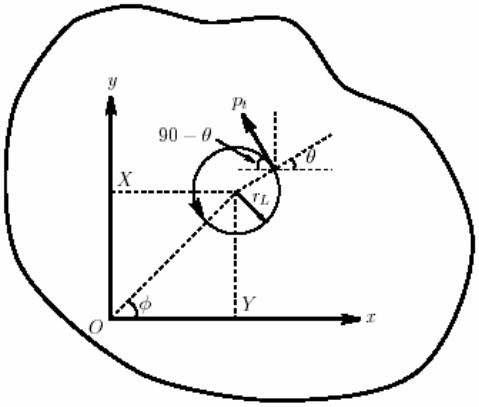

Figure 2.2: Projection of an electron orbit on the cross-sectional plane of the waveguide [28].

Performing the coordinate transformation on the equations of motion we have

$$\dot{p}'_\perp = -\frac{1}{\beta_z}\Re e\left\{A' e^{i(\omega t - k_z z)} G_\theta\right\} \tag{2.57}$$

$$p'_\perp \dot{\phi} = \frac{1}{\beta_z}\Re e\left\{A' e^{i(\omega t - k_z z)} G_r\right\} \tag{2.58}$$

$$\dot{p}'_z = -\frac{1}{\beta_z}\Re e\left\{A' e^{i(\omega t - k_z z)} G_z\right\} \tag{2.59}$$

$$\dot{X}' = \frac{1}{\beta_z}\Re e\left\{A' e^{i(\omega t - k_z z)} G_y\right\} \tag{2.60}$$

$$\dot{Y}' = -\frac{1}{\beta_z}\Re e\left\{A' e^{i(\omega t - k_z z)} G_x\right\} \tag{2.61}$$

Since the Lorentz force $\vec{G}$ is a periodic function of the angular coordinate θ, it can be represented as a Fourier series

$$\vec{G} = \sum_{l=-\infty}^{\infty} \vec{G}_l e^{-il\theta}, \qquad \text{where } \vec{G}_l = \frac{1}{2\pi}\int_0^{2\pi} \vec{G} e^{il\theta} d\theta \tag{2.62}$$

Substituting (2.62) into Eqs 2.57-2.59 one can define the following phase variable

$$\vartheta_l = \omega t - k_z \upsilon_z - l\theta \tag{2.63}$$

If we assume that the cyclotron resonance is such that $\left|\omega - k_z \upsilon_z - s\Omega\right| \ll \omega$ and the variables $p_\perp', p_z', \psi, X', Y',$ and r_L' vary slowly during the interaction between the electrons and the RF field, the equations of electron motion can be averaged over fast gyrations. In other words, the electron beam may interact with the RF field over several cyclotron periods although the electrons may take a relatively long time to travel through the interaction structure. The time it takes to execute one such period is the fast time scale. After averaging, Eqs 2.57-2.61 reduce to

$$\dot{p}_\perp' = -\frac{1}{\beta_z}\Re e\left\{A' G_{l\theta} e^{i\vartheta_l}\right\}, \tag{2.64}$$

$$p_\perp'\left[\frac{\gamma}{p_z} - h - \dot{\vartheta}_l - l\frac{\mu}{p_z'}\right] = \frac{l}{\beta_z}\Re e\left\{A' G_{lr} e^{i\vartheta_l}\right\}, \tag{2.65}$$

$$\dot{p}_z' = -\frac{1}{\beta_z}\Re e\left\{A' G_{lz} e^{i\vartheta_l}\right\}, \tag{2.66}$$

$$\dot{X}' = \frac{1}{\beta_z}\Re e\left\{A' G_{ly} e^{i\vartheta_l}\right\}, \tag{2.67}$$

$$\dot{Y}' = -\frac{1}{\beta_z}\Re e\left\{A' G_{lx} e^{i\vartheta_l}\right\}, \tag{2.68}$$

The components of the Lorentz force can be expressed through the membrane function [8]

$$\Psi(x,y)=\int_0^{2\pi}\hat{\Psi}(\varphi)e^{ik_\perp(x\cos\varphi+y\sin\varphi)}d\varphi. \tag{2.69}$$

Since Ψ is periodic in the azimuthal direction θ it can be represented as an infinite sum of harmonics as

$$\Psi(x,y)=\sum_{l=-\infty}^{\infty}\Psi_l e^{-il\theta} \qquad \text{where } \Psi_l=\frac{1}{2\pi}\int_0^{2\pi}\Psi e^{il\theta}d\theta \tag{2.70}$$

Substituting (2.69) into (2.70) gives

$$\Psi_l=\frac{1}{2\pi}\int_0^{2\pi}\left[\int_0^{2\pi}\hat{\Psi}(\varphi)e^{ik_\perp(x\cos\varphi+y\sin\varphi)}d\varphi\right]\cdot e^{il\theta}d\theta. \tag{2.71}$$

If the position of a gyrating electron is expressed as

$$x=X+r_L\cos\theta, \qquad\qquad y=Y+r_L\sin\theta, \tag{2.72}$$

the function Ψ_l becomes

$$\Psi_l=\frac{1}{2\pi}\int_0^{2\pi}\left[\int_0^{2\pi}\hat{\Psi}(\varphi)e^{ik_\perp\left[(X+r_L\cos\theta)\cos\varphi+(Y+r_L\sin\theta)\sin\varphi\right]}d\varphi\right]\cdot e^{il\theta}d\theta. \tag{2.73}$$

If we let $\bar{\theta}=\theta-\varphi$, the last integral takes the form of a Bessel function

$$\Psi_l=\int_0^{2\pi}\hat{\Psi}(\varphi)e^{ik_\perp[X\cos\varphi+Y\sin\varphi]+il\varphi}d\varphi\cdot\frac{1}{2\pi}\int_0^{2\pi}e^{i\left(k_\perp r_L\cos\bar{\theta}+l\bar{\theta}\right)}d\bar{\theta}$$

$$=\frac{1}{k_\perp}\left(\frac{\partial}{\partial X}+i\frac{\partial}{\partial Y}\right)^l\Psi\left(X,Y\right)\cdot J_l(k_\perp r_L)$$

$$=J_l(k_\perp r_L)L_l(X,Y) \tag{2.74}$$

Substituting (2.74) into (2.70) yields the following simplified form of the membrane function

$$\Psi(x,y)=\sum_{l=-\infty}^{\infty} J_l(k_\perp r_L)L_l(X,Y)e^{-il\theta}\text{, where } L_l=\frac{1}{k_\perp}\left(\frac{\partial}{\partial X}+i\frac{\partial}{\partial Y}\right)^l\Psi\left(X,Y\right). \quad (2.75)$$

Since the waveguide considered in this case has a cylindrical geometry it will be more convenient to transform the Cartesian coordinates of the guiding center X and Y to polar coordinates r, ϕ using the relation

$$X=r\cos\phi, \qquad Y=r\sin\phi. \quad (2.76)$$

The differential operator in L_l can be transformed as well to polar coordinates as follows

$$\frac{\partial}{\partial X}=\cos\phi\frac{\partial}{\partial r}-\frac{\sin\phi}{r}\frac{\partial}{\partial\phi},$$
$$\frac{\partial}{\partial Y}=\sin\phi\frac{\partial}{\partial r}+\frac{\cos\phi}{r}\frac{\partial}{\partial\phi}$$

to obtain

$$L_l=\left\{e^{i\phi}\frac{1}{k_\perp}\left(\frac{\partial}{\partial r}+i\frac{\partial}{\partial\phi}\right)\right\}^l\Psi\left(r,\phi\right) \quad (2.77)$$

From the previous derivation in Section 2.3.2 one can deduce that the membrane function for a $TE_{m,p}$ mode in a cylindrical waveguide must be of the form $J_m(k_\perp r)e^{\mp m\phi}$. The transverse wavenumber $k_\perp$ is determined in (2.20): $k_\perp=\nu_{mp}/R_w$ where R_w is the waveguide radius, and ν_{mp} is the p-th root of the equation $dJ_m(\nu)/d\nu=0.$ Using the recurrent relation $dJ_m(x)/dx=\frac{m}{x}J_m(x)-J_{m+1}(x)$, one can show that the differential operator given by (2.77) is equal to

$$L_l=J_{m\mp l}(k_\perp r)e^{i(l\mp m)\phi} \quad (2.78)$$

where $m-l$ and $m+l$ correspond to the co- and counter rotating waves with respect to electron gyration, respectively.

For TE waves, the axial component of the magnetic field H_z can be represented as

$$H_z = i\Psi \,. \tag{2.79}$$

Then, from Eqs 2.6 to 2.9 we obtain the following transverse field components in terms of the membrane function

$$H_r = \frac{k_z}{k_\perp^2}\frac{\partial \Psi}{\partial r} \tag{2.80}$$

$$E_\theta = -\frac{k}{k_\perp^2}\frac{\partial \Psi}{\partial r} \tag{2.81}$$

$$H_\theta = \frac{k_z}{k_\perp^2 r}\frac{\partial \Psi}{\partial \theta} \tag{2.82}$$

$$E_r = \frac{k}{k_\perp^2 r}\frac{\partial \Psi}{\partial \theta}, \tag{2.83}$$

Substituting these expressions into (2.45) yields

$$G_{r_L} = \frac{k}{k_\perp^2 r_L}(1-h\beta_z)\frac{\partial \Psi}{\partial \theta} + i\beta_\perp \frac{k^2}{k_\perp^2}\Psi \tag{2.84}$$

$$G_\theta = -\frac{k}{k_\perp^2}(1-h\beta_z)\frac{\partial \Psi}{\partial r} \tag{2.85}$$

$$G_z = -\beta_\perp \frac{k_z}{k_\perp^2}\frac{\partial \Psi}{\partial r} \tag{2.86}$$

Recalling the constraint on k_z from (2.25): $k_z \ll k$ or $k_\perp \simeq k$, we can simplify the last equations as follows

$$G_{r_L} \simeq \frac{1}{k_\perp r_L}\frac{\partial \Psi}{\partial \theta} + i\beta_\perp \Psi \tag{2.87}$$

$$G_\theta \simeq -\frac{1}{k_\perp}\frac{\partial \Psi}{\partial r} \tag{2.88}$$

$$G_z \simeq 0 \tag{2.89}$$

Replacing Ψ by its full expression given in (2.75) and substituting into (2.44), the equations of electron motion (2.64-66) become

$$\dot{p}'_\perp = \frac{1}{\beta_z}\Re e\left\{ A' e^{i(\omega t - k_z z)} \sum_{l=1}^{3} J'_l(k_\perp r_L) L_l e^{-il\theta} \right\} \tag{2.90}$$

$$p'_\perp \left[\dot{\theta} - \frac{\mu}{p'_z} \right] = \frac{1}{\beta_z}\Re e\left\{ iA' e^{i(\omega t - k_z z)} \sum_{l=1}^{3} \left(\beta_\perp - \frac{l}{k_\perp r_L} \right) J_l(k_\perp r_L) L_l e^{-il\theta} \right\} \tag{2.91}$$

$$\dot{p}'_z = 0 \tag{2.92}$$

The last equation shows that the axial momentum of the electron remains essentially unchanged through out the interaction with the RF field (i.e., $p_z = p_{z0}$). Notice that the possibility of overlapping of resonances is accounted here by the superposition of several harmonics of the membrane function.

Having derived the equations describing the electron phase and orbital momentum we now turn to the evolution of the electron energy, $\mathcal{E} = m_\circ c^2 \gamma$, along the axial length,

$$\frac{d\mathcal{E}}{dt} = -e\left(\vec{\upsilon} \cdot \vec{E}\right). \tag{2.93}$$

Using normalized variables the last equation can be expressed as

$$\frac{d\gamma}{dz'} = -\left(\frac{\vec{\upsilon}_\perp}{\upsilon_z} \cdot \frac{e\vec{E}_\theta}{m_0 c\omega} \right). \tag{2.94}$$

From (2.81) and (2.94) we have

$$\frac{d\gamma}{dz'} = \frac{p'_\perp}{p'_{z0}} \Re e\left\{ A' e^{i(\omega t - k_z z)} \sum_{l=1}^{3} J'_l(k_\perp r_L) L_l e^{-il\theta} \right\}, \tag{2.95}$$

We can rearrange equation 2.91 as follows

$$\frac{d\theta}{dz'} = \frac{\mu}{p'_{z_0}} + \frac{1}{p'_\perp \beta_z} \Re e\left\{ iA' e^{i(\omega t - k_z z)} \sum_{l=1}^{3} \left(\beta_\perp - \frac{l}{k_\perp r_L} \right) J_l(k_\perp r_L) L_l e^{-il\theta} \right\}. \tag{2.96}$$

Here and below we normalize all parameters with respect to the initial electron energy γ_0 as follows

$$\hat{\gamma} = \gamma / \gamma_0, \quad \hat{p}_\perp = p'_\perp / \gamma_0, \quad \hat{\mu} = \mu / \gamma_0 = \Omega_0 / \omega, \quad \hat{A} = A' / \gamma_0, \tag{2.97}$$

and introduce the following normalized axial length

$$\xi = \frac{z'}{\beta_{z0}} = \frac{\omega z}{c\beta_{z0}}. \tag{2.98}$$

The phase and energy equations 2.97 and 2.98 become

$$\frac{d\hat{\gamma}}{d\xi} = \hat{p}_\perp \Re e\left\{ \hat{A} e^{i(\omega t - k_z z)} \sum_{l=1}^{3} J'_l(k_\perp r_L) L_l e^{-il\theta} \right\} \tag{2.99}$$

$$\frac{d\theta}{d\xi} = \hat{\mu} + \Re e\left\{ i\hat{A} e^{i(\omega t - k_z z)} \sum_{l=1}^{3} \left(1 - \frac{l}{k_\perp r_L \beta_\perp} \right) J_l(k_\perp r_L) L_l e^{-il\theta} \right\}. \tag{2.100}$$

In this normalization the electron energy and momentum are related through $\gamma^2 = \gamma_0^{-2} + p_\perp^2 + p_z^2$ where we have left the "hats" out. If we introduce the following phase variable

$$2\varphi = \omega t - k_z z - 2\theta \quad \text{where} \quad \theta = \theta_0 + \mu\xi \tag{2.101}$$

then, $\frac{d\varphi}{d\xi} = \frac{\omega}{2}\frac{d\tau}{d\xi} - \frac{1}{2}\frac{dz}{d\xi} - \frac{d\theta}{d\xi} = \frac{\gamma}{2} - \frac{1}{2}h\beta_{z0} - \frac{d\theta}{d\xi}$

$$= \frac{\gamma - 1}{2} + \Delta - \Re e\left\{ iFe^{i2\varphi}\left[\left(1 - \frac{\mu\gamma}{\kappa p_\perp^2}\right) J_1(\hat{a}) b_1 e^{i\theta} + \left(1 - \frac{2\mu\gamma}{\kappa p_\perp^2}\right) J_2(\hat{a}) + \left(1 - \frac{3\mu\gamma}{\kappa p_\perp^2}\right) J_3(\hat{a}) b_3 e^{-i\theta}\right]\right\} \tag{2.102}$$

$$\frac{d\gamma}{d\xi} = p_\perp \Re e\left\{ Fe^{i2\varphi}\left[J_1'(\hat{a}) b_1 e^{i\theta} + J_2'(\hat{a}) + J_3'(\hat{a}) b_3 e^{-i\theta}\right]\right\} \tag{2.103}$$

Here $\Delta = (1 - h\beta_{z0})/2 - \mu$ is the cyclotron resonance detuning or initial synchronism mismatch, $F = eAL_2 / \gamma_0 m_0 c\omega$ is the normalized field amplitude, the argument of the Bessel function is defined as $\hat{a} = k_\perp r_L = k_\perp c\beta_\perp / \Omega = \kappa p_\perp / \mu$, $\kappa = k_\perp / k$ is the normalized transverse wave number, and $b_{1,3} = \left| L_{1,3} / L_2 \right|$ is the ratio of the coupling impedances of electrons to the wave at different cyclotron harmonics.

Having derived the equations describing the evolution of the electron phase and energy in terms of the field amplitude, it is expedient to express the evolution of the field amplitude in terms of the electron energy and phase as well.

2.3.3 Field amplitude in terms of beam current

We return to equation (2.36) and rewrite it in terms of the normalized axial length (2.98). It becomes

$$\frac{\partial A}{\partial \xi} + \frac{1}{\beta_{gr}} \frac{\partial A}{\partial t'} = \frac{I_0}{k_z N_s} \frac{1}{2\pi} \int_0^{2\pi} e^{-i(\omega t - k_z z)} \vec{p}_\perp \cdot \vec{E}_\theta^* d\left(\omega t_0\right) \tag{2.104}$$

where $\beta_{gr} = \upsilon_{gr} / c$ is the wave group velocity normalized to the speed of light, $t' = \omega t / \beta_{z0}$ is the normalized time variable, and I_0 is the DC beam current defined as

$$\int_{S_\perp} j_{z0} dS_\perp = -I_0 \tag{2.105}$$

Expressing E_θ in terms of the membrane function and using normalization (2.101) equation (2.104) becomes

$$\frac{\partial A}{\partial \xi}+\frac{1}{\beta_{gr}}\frac{\partial A}{\partial t'}=\frac{-eI_0}{m_o c^2}\frac{k_\perp^{-1}}{hN_s}\frac{1}{2\pi}\int_0^{2\pi} p_\perp e^{-i2\varphi}L_2^*\left[J_1'(\hat{a})b_1e^{-i\theta}+J_2'(\hat{a})+J_3'(\hat{a})b_3e^{i\theta}\right]d\varphi_0 \quad (2.106)$$

where the norm N_s of the wave defined in (2.35) can be determined more explicitly using the transverse field components. For our cylindrical structure we obtain

$$N_s=\frac{c}{4}\frac{k^2}{k_\perp^3}\left(\nu^2-m^2\right)J_m^2(\nu) \quad (2.107)$$

If both sides of equation (2.106) are multiplied by L_2 it becomes

$$\frac{\partial F}{\partial \xi}+\frac{1}{\beta_{gr}}\frac{\partial F}{\partial t'}=-\frac{I}{2\pi}\int_0^{2\pi} p_\perp e^{-i2\varphi}\left[J_1'(\hat{a})b_1e^{-i\theta}+J_2'(\hat{a})+J_3'(\hat{a})b_3e^{i\theta}\right]d\varphi_0 \quad (2.108$$

where the normalized current is given by

$$I=\frac{I_0}{N_s k_z}=4\frac{eI_0}{m_0c^3}\frac{\kappa^2 J_{m-p}^2(k_\perp R_w)}{h\left(\nu^2-m^2\right)J_m^2(\nu)} \quad (2.109)$$

The two-dimension envelope equation (2.108) can be reduced to one-dimension through the following steps: first, we introduce a new time variable

$$t''=t'-\frac{\xi}{\beta_{z0}}, \quad (2.110)$$

which transforms the left hand side (LHS) of the envelope equation into:

$$\frac{\partial F}{\partial \xi}+\frac{1}{\beta_{gr}}\frac{\partial F}{\partial t'}=\frac{\partial F}{\partial \xi}+\left(\frac{1}{\beta_{gr}}-\frac{1}{\beta_{z0}}\right)\frac{\partial F}{\partial t''}. \quad (2.111)$$

Then, we introduce $\tau=\left(t'-\frac{\xi}{\beta_{z0}}\right)\left(\frac{1}{\beta_{gr}}-\frac{1}{\beta_{z0}}\right)^{-1}$ where $t'=\frac{\omega t}{\beta_{z0}}$ (2.112)

Substituting (2.112) into (2.111) yields

$$\frac{\partial F}{\partial \xi}+\frac{1}{\beta_{gr}}\frac{\partial F}{\partial t'}=\frac{\partial F}{\partial \xi}+\frac{\partial F}{\partial \tau}. \tag{2.113}$$

Finally, if we combine the time and length variables into characteristic $u=\tau-\xi$, it can easily be shown that

$$\frac{\partial F}{\partial \xi}+\frac{\partial F}{\partial \tau}=\frac{\partial F}{\partial \xi} \tag{2.114}$$

Therefore, the envelope equation reduces to

$$\frac{\partial F}{\partial \xi}=-\frac{I}{2\pi}\int_0^{2\pi} p_\perp e^{-i2\varphi}\left[J_1'(\hat{a})b_1e^{-i\theta}+J_2'(\hat{a})+J_3'(\hat{a})b_3e^{i\theta}\right]d\varphi_0\,, \tag{2.115}$$

which along with equations (2.102) - (2.103) form a self consistent set of equations describing simultaneous resonance interaction at several harmonics in our gyro-TWA amplifier model. It can be shown with the use of these equations that the energy is conserved in this interaction as described by the following relation

$$|F|^2-|F_0|^2=\left(1-\gamma_0^{-1}\right)\eta I\,, \tag{2.116}$$

where F_0 is the initial field amplitude and η is the efficiency of the electron beam-wave interaction,

$$\eta=\frac{\left(1-\langle\gamma\rangle\right)}{\left(1-\gamma_0^{-1}\right)}. \tag{2.117}$$

The angular brackets mean averaging over initial phases φ_0.

2.4 Mode interaction theory

2.4.1 Description of wave interaction mechanism

In a typical gyro-traveling-wave amplifier, a signal with frequency ω_s is fed into the waveguide. This signal excites a waveguide mode, which then interacts with

the electron beam. Waveguide modes with frequencies at harmonics of the signal frequency can also get excited. In multistage devices such as the gyrotwystron the electron beam gets modulated in the input stage by the signal at frequency ω_s, then in the drift section separating the input stage with the output stage, high-frequency components in the current density arise. Therefore, the output stage can operate at harmonics of ω_s. In other words, the excitation of one wave can result in the excitation of other waves through a nonlinear process sustained by the presence of the electron beam. This effect has been extensively studied in gyrotron oscillators (see for example [21-23, 29] and refs. therein). Here we study the interaction between three traveling waves in gyro-amplifiers. The waves considered are the so-called symmetric $TE_{0,p}$ waves whose frequencies and wave vectors obey the following general synchronism conditions [29]:

$$\omega_1 + \omega_2 = \omega_3, \qquad \vec{k}_1 + \vec{k}_2 = \vec{k}_3. \tag{2.118}$$

The condition for the wave vectors can be written more specifically for gyro traveling-wave devices as

$$m_1 + m_2 = m_3\,, \tag{2.119}$$

and

$$k_{1z} + k_{2z} \approx k_{3z}\,, \tag{2.120}$$

In (2.119) m_s are azimuthal indices of non-symmetric waves rotating in a circular waveguide.

The condition of synchronism between axial wavenumbers (2.120) is absent in gyrotron oscillators, which operate at frequencies close to cutoff. In gyro-traveling-wave devices, this condition holds only for some specific waves as illustrated in the

dispersion diagram shown in Figure 2.3, which is similar to Figure 2.1. Here the uncoupled dispersion diagram is plotted for three waves TE_{01}, TE_{02} and TE_{03} interacting with gyrating electrons at the fundamental, second and third cyclotron resonance harmonics, respectively. The TE_{01} wave is excited first by a signal at frequency ω_s. Then, as it is the case in amplifiers, two other waves are excited at $2\omega_s$ (TE_{02}-wave) and $3\omega_s$ (TE_{03}-wave). These frequencies are shown in Figure 2.3 by dotted horizontal lines. As one can see, the intersection of these lines with dispersion curves for the waveguide modes takes place at a certain distance from the straight lines showing the cyclotron resonance at corresponding harmonics. This departure from the exact cyclotron resonance is more pronounced for the second and third waves, and should result in weak excitation of these waves.

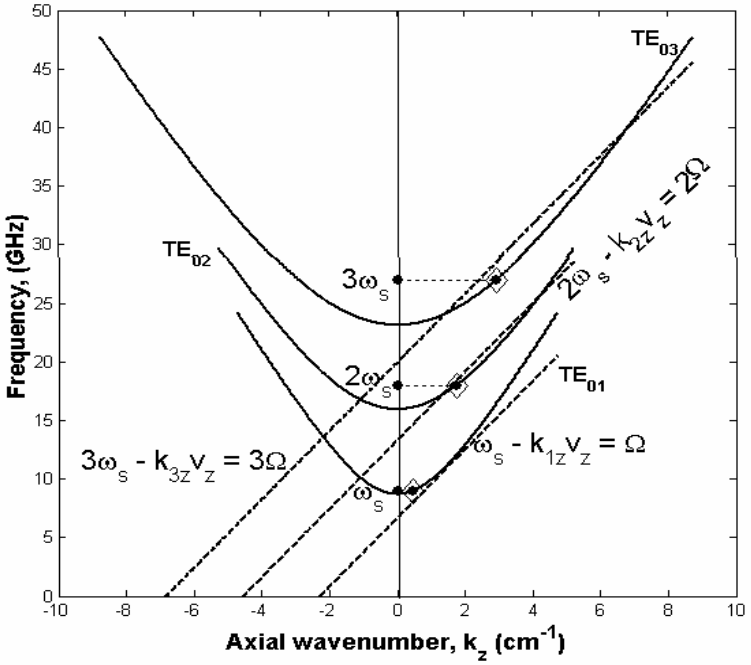

Figure 2.3: Dispersion diagram when the magnetic field is optimal for the fundamental harmonic interaction. Diamonds indicate the operating points for all three waves at corresponding harmonics of the signal frequency.

2.4.2 Equations describing wave interaction

In this case the electric field is represented as a superposition of three transverse electric modes TE_{01}, TE_{02}, and $TE_{03,}$ which satisfy the synchronism conditions (2.118-120)

$$\vec{E} = \Re e\left\{\sum_{s=1}^{3} A_s(z,t)\vec{E}_s(\vec{r}_\perp)e^{i(\omega_s t - k_{sz} z)}\right\}. \tag{2.121}$$

The equations of wave excitation and electron motion are derived in a similar manner as in the case of single wave interaction using the same constraint on the axial wave number of each of the modes: $\pi/L \ll k_{sz} \ll \omega_s/c$. Here, the index *s* instead of *m,p* is used to label modes for simplicity.

The evolution of each of the waves is described by an equation similar to (2.115).

$$\frac{dF_1}{d\xi} = -\frac{I_1}{2\pi}e^{-i\delta_1\xi}\int_0^{2\pi}\frac{p_\perp}{2}e^{-i\varphi}\left[1 + b_2\frac{p_\perp}{2}e^{i\theta} + b_3\frac{p_\perp^2}{8}e^{i2\theta}\right]d\varphi_0\,, \tag{2.122}$$

$$\frac{dF_2}{d\xi} = -\frac{I_2}{2\pi}\int_0^{2\pi}\frac{p_\perp}{2}e^{-i2\varphi}\left[b_1e^{-i\theta} + p_\perp + b_3\frac{p_\perp^2}{2}e^{i\theta}\right]d\varphi_0\,, \tag{2.123}$$

$$\frac{dF_3}{d\xi} = -\frac{I_3}{2\pi}e^{-i\delta_3\xi}\int_0^{2\pi}\frac{p_\perp}{2}e^{-i3\varphi}\left[b_1e^{-i2\theta} + b_2\frac{3p_\perp}{2}e^{-i\theta} + \frac{9}{8}p_\perp^2\right]d\varphi_0\,, \tag{2.124}$$

where it is assumed that the external magnetic field is tuned such that the second harmonic interaction is the dominant interaction. Therefore, the first and third waves are shifted in phase with respect to the second wave as indicated by the parameters δ_1 and δ_3, which are defined in (2.125) and (2.126) below. The Bessel functions of

the normalized Larmor radius $\hat{a}$ have been replaced by their polynomial expansions. The ratio of the coupling impedances of electrons to the wave is given by $b_{1,2,3} = \left| L_{1,2,3} / L_s \right|$. For a given wave one of the b parameters, which corresponds to the dominant cyclotron resonance is equal to unity, $b_s = 1$. The variable $\varphi = \left(\omega_2 t - k_{2z} z \right) / 2 - \theta$ is the phase of the wave with respect to the electron gyrophase for the second harmonic resonance. Using this phase definition we have

$$\begin{aligned} \omega_1 - k_{1z} z - \theta &= \varphi + (k_{2z} / 2 - k_{1z}) z \\ &= \varphi + \beta_{z0} \left\{ \sqrt{1 - \left(\frac{\nu_{02}}{2\hat{R}} \right)^2} - \sqrt{1 - \left(\frac{\nu_{01}}{\hat{R}} \right)^2} \right\} \xi \\ &= \varphi + \delta_1 \xi \end{aligned} \tag{2.125}$$

$$\begin{aligned} \omega_3 - k_{3z} z - 3\theta &= 3\varphi + (3k_{2z} / 2 - k_{3z}) z \\ &= 3\varphi + 3\beta_{z0} \left\{ \sqrt{1 - \left(\frac{\nu_{02}}{2\hat{R}} \right)^2} - \sqrt{1 - \left(\frac{\nu_{03}}{3\hat{R}} \right)^2} \right\} \xi \\ &= 3\varphi + \delta_3 \xi \end{aligned} \tag{2.126}$$

where $\hat{R} = \omega_1 R_w / c$ is the normalized waveguide wall radius , ν_{01}, and ν_{03} are the TE_{01} and TE_{03} waves eigenvalues, respectively.

The equations describing the evolution of the normalized electron energy and phase are also derived following the same steps as in Section 2.3. They account for the fact that the beam interacts with all three waves, and for each of these waves the overlapping of resonances is possible

$$\frac{d\gamma}{d\xi} = \frac{p_\perp}{2} \Re e \left\{ F_1 e^{i(\varphi + \delta_1 \xi)} \left[1 + b_2 \frac{p_\perp}{2} e^{-i\theta} + b_3 \frac{p_\perp^2}{8} e^{-i2\theta} \right] + F_2 e^{i2\varphi} \left[b_1 e^{i\theta} + p_\perp + b_3 \frac{p_\perp^2}{2} e^{-i\theta} \right] \right.$$

$$+F_3 e^{i(3\varphi+\delta_3\xi)}\left[b_1 e^{i2\theta}+b_2\frac{3p_\perp}{2}e^{i\theta}+\frac{9}{8}p_\perp^2\right]\Bigg\} \tag{2.127}$$

$$\frac{d\varphi}{d\xi}=\gamma-1+\Delta-\Re e\Bigg\{iF_1e^{i(\varphi+\delta_1\xi)}\left[\left(1-\frac{\gamma}{p_\perp^2}\right)\frac{p_\perp}{2}+b_2\left(1-\frac{2\gamma}{p_\perp^2}\right)\frac{p_\perp^2}{8}e^{-i\theta}+b_3\left(1-\frac{3\gamma}{p_\perp^2}\right)\frac{p_\perp^3}{48}e^{-i2\theta}\right]$$

$$+iF_2e^{i2\varphi}\left[b_1\left(1-\frac{\gamma}{2p_\perp^2}\right)p_\perp e^{i\theta}+\left(1-\frac{\gamma}{p_\perp^2}\right)\frac{p_\perp^2}{2}+b_3\left(1-\frac{3\gamma}{2p_\perp^2}\right)\frac{p_\perp^3}{6}e^{-i\theta}\right]$$

$$+iF_3e^{i(3\varphi+\delta_3\xi)}\left[b_1\left(1-\frac{\gamma}{3p_\perp^2}\right)\frac{3p_\perp}{2}e^{i2\theta}+b_2\left(1-\frac{2\gamma}{3p_\perp^2}\right)\frac{9p_\perp^2}{8}e^{i\theta}+\left(1-\frac{\gamma}{p_\perp^2}\right)\frac{9p_\perp^3}{16}\right]\Bigg\} \tag{2.128}$$

Here also, the electron energy γ is normalized to its initial value γ_0, and the cyclotron resonance detuning is defined as $\Delta=1-h_2\beta_{z_0}-\mu$. The normalized electron energy and momentum are related as $\gamma^2=\gamma_0^{-2}+p_\perp^2+p_z^2$. The set of equations (2.122-126 and 2.127-128) describe the interaction between modes when the overlapping of cyclotron resonances is also likely. Note that in the absence of the overlapping of cyclotron resonances, i.e. when $b=0$, these equations are greatly simplified.

It is also possible to show in this case that the envelope equations (2.122-124) together with the normalized electron energy and phase equations (2.127) – (2.128) form a set of self-consistent equations. The equation describing the energy exchange between the waves and the beam is given by

$$I_1^{-1}\left(|F_1|^2-|F_1(0)|^2\right)+I_2^{-1}\left(|F_2|^2-|F_2(0)|^2\right)+I_3^{-1}\left(|F_3|^2-|F_3(0)|^2\right)=2(1-\gamma_0^{-1})\eta, \tag{2.129}$$

where $F_s(0)$ is the initial amplitude of a given wave and η is the efficiency of the electron beam-wave interaction previously defined in (2.117) above.

2.5 Summary

In this Chapter, equations describing the interaction between relativistic electrons and the RF field in a gyro-traveling wave amplifier have been derived for the case when the axial wave number k_z is large enough to neglect electron interaction with backward waves, but small enough to neglect the changes in electron axial momentum. These equations also account for the possibility of the overlapping of resonances at the first three cyclotron harmonics. Equations describing the nonlinear interaction between three symmetric waveguide modes were also presented. In the next three chapters the results of numerical simulations of these equations are presented and discussed.

Chapter 3: Effect of Cyclotron Resonances Overlapping on Electron Trajectories

3.1 Introduction

In this Chapter we consider a simplified form of the model discussed in Section 2.3 in order to illustrate the effect of the overlapping of cyclotron resonances on electron trajectories. Here we assume that relativistic electrons interact with a constant large amplitude electromagnetic wave with a negligible axial wavenumber. Therefore, the system is described by equations (2.102) and (2.103)

$$\frac{d\varphi}{d\xi}=\frac{\gamma-1}{2}+\Delta-\Re e\left\{iFe^{i2\varphi}\left[\left(1-\frac{\mu\gamma}{p_\perp^2}\right)J_1(\hat{a})b_1e^{i\theta}+\left(1-\frac{2\mu\gamma}{p_\perp^2}\right)J_2(\hat{a})+\left(1-\frac{3\mu\gamma}{p_\perp^2}\right)J_3(\hat{a})b_3e^{-i\theta}\right]\right\}$$

$$\frac{d\gamma}{d\xi}=p_\perp\Re e\left\{Fe^{i2\varphi}\left[J_1'(\hat{a})b_1e^{i\theta}+J_2'(\hat{a})+J_3'(\hat{a})b_3e^{-i\theta}\right]\right\}, \tag{3.1}$$

where the cyclotron resonance detuning is reduced to $\Delta=1/2-\mu$. As before, the normalized electron energy and momentum are related through $\gamma^2=\gamma_0^{-2}+p_\perp^2+p_z^2$. Therefore, at the entrance to the output waveguide we have $\gamma(0)=1$, and $p_\perp(0)=\beta_{\perp0}$. It is important to mention that equations (3.1) describe a Hamiltonian system. They can be expressed via the following Hamiltonian for the case $b_1=b_3=0$ [26]:

$$H=-\frac{1}{4}(\gamma-1)^2+(1/2-\mu)(\gamma-1)-\frac{p_\perp}{2}\Re e\left\{iFe^{i2\varphi}J_2'(2p_\perp)\right\} \tag{3.2}$$

The set of ordinary differential equations (3.1) was solved simultaneously using standard numerical technique. Below we first present and analyze the

simulation results. Next, using the Lyapunov exponent approach we attempt to prove that electron trajectories are really stochastic. Finally, the Chapter is concluded.

3.2 Simulation results

Equations (3.1) were solved for the initial ratio of the orbital velocity to the axial velocity, $\alpha = 1$, normalized wave amplitude $F = 0.3$, and zero detuning (i.e. $\mu = 0.5$). Figure 3.1 shows the normalized transverse momentum of electrons for the coupling impedance parameter $b = b_1 = b_3 = 0,\ 0.1$, and 0.3.

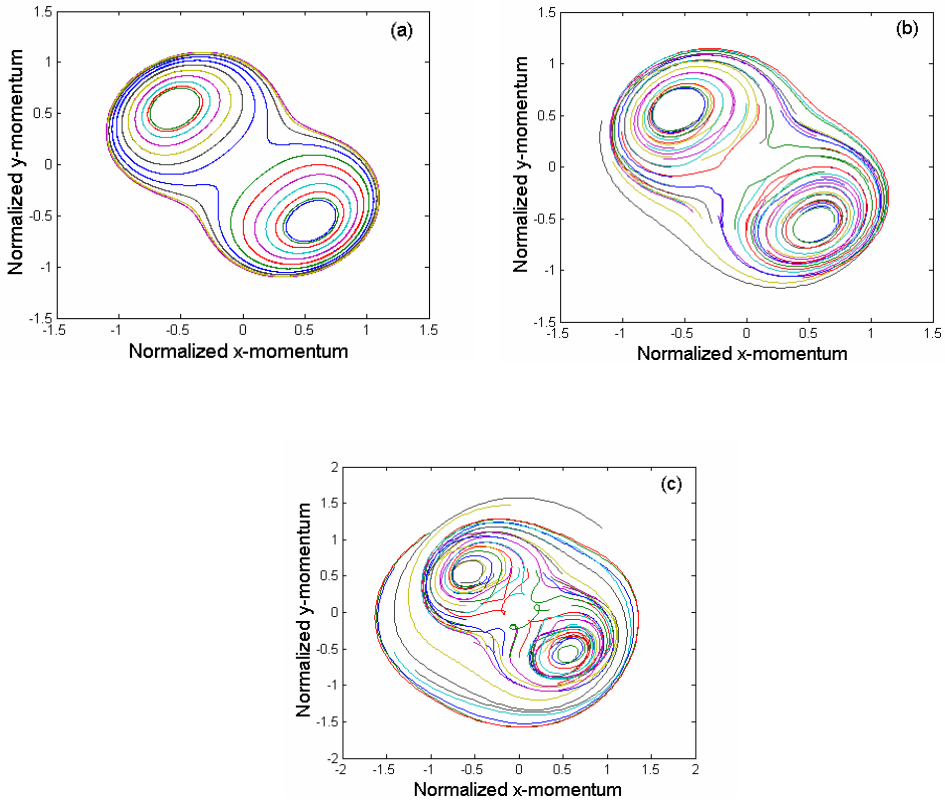

Figure 3.1: Plots of electron transverse momentum in Cartesian coordinates $p_x = p_\perp \cos\theta \quad p_y = p_\perp \sin\theta$ **for (a)** $b = 0$**, (b)** $b = 0.1$**, and (c)** $b = 0.3$

It is apparent in Figure 3.1 that as the value of the parameter *b* increases the electrons exhibit less regular trajectories. A similar conclusion can be drawn from Figure 3.2 showing the axial dependence of electron phases for $b = b_1 = b_3 = 0, .0.3$, and 0.5.

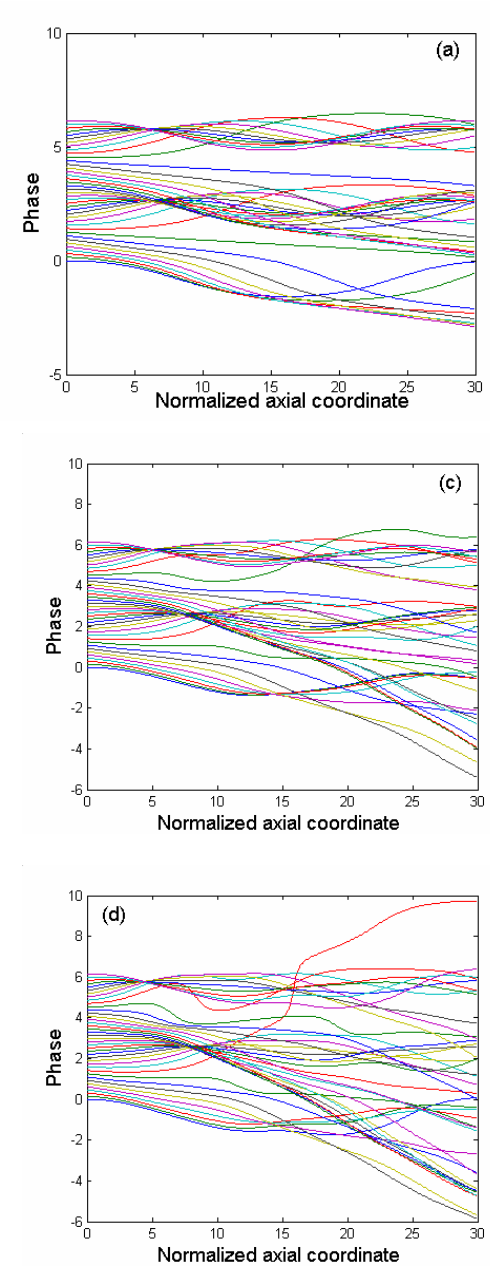

Figure 3.2: Electron phase plot for $b = b_1 = b_3 = 0$, 0.3, and 0.5.

One can observe from Figure 3.2 that for *b = 0* two electron bunches are visible, but as the value of *b* increases the bunches are destroyed as electrons move from one bunch to the other. In order to better illustrate the chaotic nature of electron trajectories we plot the Poincaré sections from the electron transverse momentum components. These allow us to identify electrons, which remain in the invariant phase space. Recalling that $\theta = \mu\xi$ and the fact that electrons form two bunches shifted by π for the case of pure second harmonic interaction, we can show that the Poincaré sections are $\Delta\xi = 2\pi$ apart. Therefore, using a long axial length realization we were able to plot Poincaré sections corresponding to several electron entrance phases as shown in Figure 3.3. There the sections are shown for $\xi_{end} = 471$ and entrance phases $\theta_0 = 0,\ \pi/2,\ \pi$, and $3\pi/2$ when *b = 0* (a) and *b = 0.5* (b). Note the complete destruction of the Poincare section periodicity as the parameter *b* value changes from 0 to 0.5

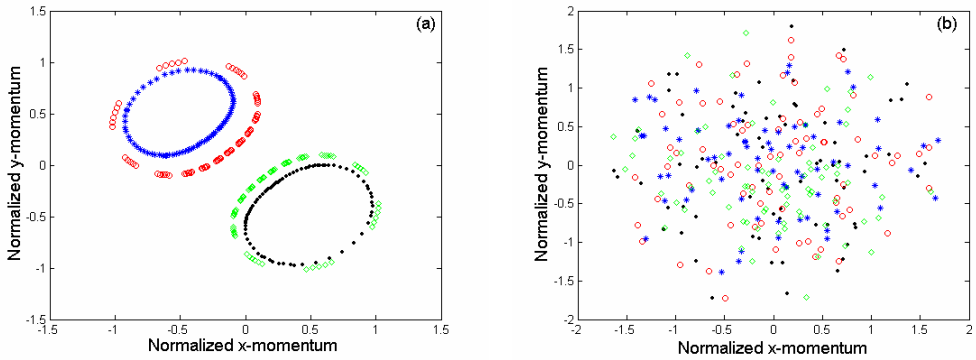

Figure 3.3: Poincare sections for electron entrance phase $\theta_0 = 0$ (black solid circles), $\theta_0 = \pi/2$ (red circles), $\theta_0 = \pi$ (blue stars), and $\theta_0 = 3\pi/2$ (green diamonds) when (a) *b = 0,* (b) *b = 0.5*

This effect is present even at smaller value of μ (or positive detuning). Figure 3.4 shows the Poincaré sections and electron transverse momentum plots for $\mu = 0.35$ when $b = 0$. Figure 3.5 shows similar results for $\mu = 0.285$ and $b = 0.5$

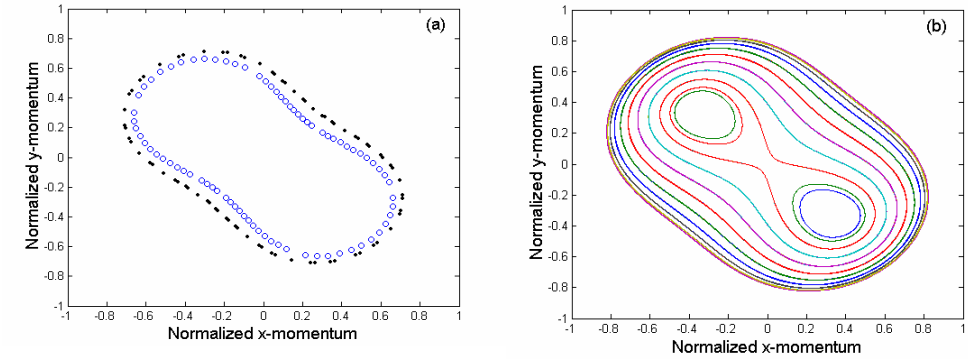

Figure 3.4: (a) Poincaré sections for electron entrance phase $\theta_0 = 0$ (black filled circles), $\theta_0 = \pi$ (blue circles), (b) normalized electron transverse momentum *b = 0*, and $\mu = 0.35$ in both (a) and (b).

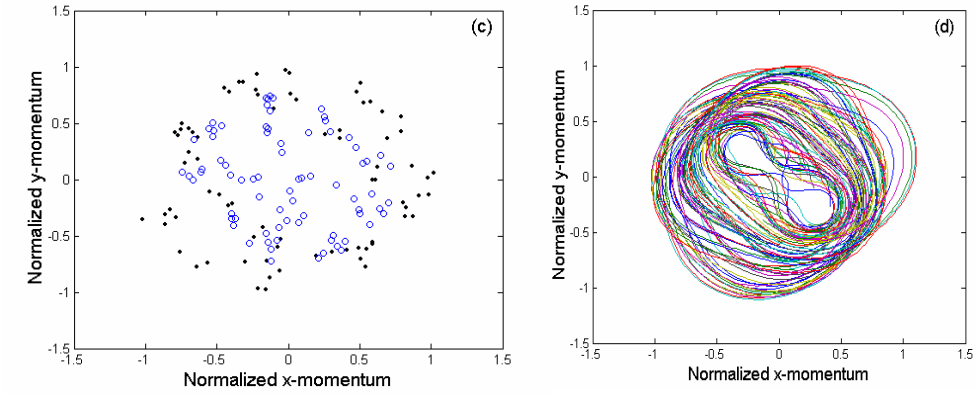

Figure 3.5: (c) Poincaré sections for electron entrance phase $\theta_0 = 0$ (black filled circles), $\theta_0 = \pi$ (blue circles), (d) normalized electron transverse momentum; *b = 0.5*, and $\mu = 0.285$ in both (c) and (d).

The effect of the overlapping of resonances on the efficiency of the interaction between the beam and the wave was also investigated. Figure 3.6 shows the dependence of the maximum efficiency on the normalized frequency ratio μ for several values of the parameter *b*.

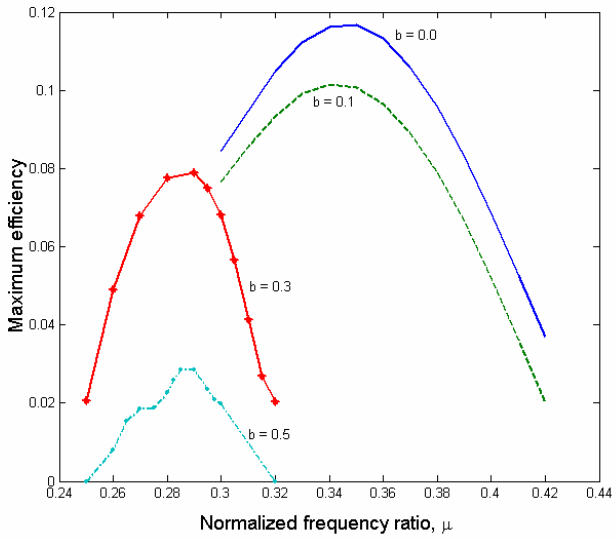

Figure 3.6: Maximum efficiency with respect to normalized frequency ratio. The maximum efficiency drops for higher b values.

One can observe that the overlapping of cyclotron resonances deteriorate the maximum efficiency of the device. The maximum efficiency is also achieved at lower values of the frequency ratio as the value of *b* increases.

3.3 Analysis of simulation results

In order to better explain the nature of electron trajectories shown above it is expedient to recall the illustration of the overlapping of cyclotron resonances in

Figure 1.4. When electrons interact with the wave at an isolated resonance (*b = 0*), they remain within a given resonance band and execute more or less regular trajectories. For instance, when $\mu = 0.5$ (i.e., $\omega \approx 2\Omega_0$), the isolated resonance interaction corresponds to the beam and the wave resonating at the second harmonic cyclotron resonance. The transverse field has a quadrupole structure as shown in Figure 1.3(b). The resonance band has two equal size lobes. This explains the presence of two symmetric electron-bunches shifted by π in Figures 3.1-4(a) above. When other harmonics are added (i.e., $b \neq 0$) the transverse field structure loses its symmetry. Therefore, some electrons can be trapped in the resonance band of the first and third harmonics. This explains the rather chaotic nature of electron trajectories as the value of *b* increases. For smaller values of μ, the interaction between the wave and the electrons takes place at higher order harmonics of the cyclotron frequency. It was noticed that, in these cases also the overlapping of cyclotron resonances could result in stochastic electron trajectories.

Some important observations can be made from the efficiency plot in Figure 3.6 as well. It is clear from the previous figures that the addition of other harmonics reduces the number of electrons interacting with the wave at the initial cyclotron resonance. This explains the decrease in efficiency as the overlapping of resonances becomes stronger with larger *b* values. It is important to mention that this effect on efficiency was also noted in [16]. One can also see that, as the value of *b* increases, the most efficient interaction occurs at lower values of the normalized frequency ratio.

Although the electron trajectories appear stochastic when the overlapping of cyclotron resonances is considered it is important to show this analytically. In the next section we do so using the Lyapunov exponent approach.

3.4 Analysis of electron trajectories using Lyapunov exponent

One method often used to check whether a system is chaotic is the Lyapunov exponent. It is a measure of the divergence or convergence of two orbits starting with slightly different initial values [30, 31]. For stationary state the Lyapunov exponent is zero. For converging orbits the Lyapunov exponent is negative while positive Lyapunov exponents indicate possible stochastic trajectories. In this study we limited our investigation to the isolated resonance case because the results above indicate stationary behavior of electrons.

Four hundred particles initially distributed in phase uniformly from 0 to 2π were considered. Each of these particles had two satellites: one initially perturbed in phase and the other initially perturbed in energy. Therefore, in the phase space representation we had initially:

$$\left(\gamma_{0,}\varphi_0\right),\ \left(\gamma_0,\varphi_0+\delta\varphi_0\right),\ \left(\gamma_0+\delta\gamma_0,\varphi_0\right) \tag{3.3}$$

where $\delta\gamma_0=\delta\varphi_0=10^{-6}$

The change in energy ($\delta\gamma$) and phase ($\delta\varphi$) at any position ξ is obtained through the following relation,

$$\begin{pmatrix}\delta\gamma\\ \delta\varphi\end{pmatrix}=\begin{pmatrix}\gamma_2 & \gamma_3\\ \varphi_2 & \varphi_3\end{pmatrix}\begin{pmatrix}\delta\gamma_0\\ \delta\varphi_0\end{pmatrix} \tag{3.4}$$

where the indices 2 and 3 represents the perturbed energy and phase, respectively. The Lyapunov exponent is defined as follows

$$h = \frac{1}{\xi}\ln\left(|\lambda|\right) \tag{3.5}$$

where λ is an eigen value of the matrix

$$\begin{bmatrix} \frac{\gamma_2 - \gamma_1}{\delta\gamma_0} & \frac{\gamma_3 - \gamma_1}{\delta\varphi_0} \\ \frac{\varphi_2 - \varphi_1}{\delta\gamma} & \frac{\varphi_3 - \varphi_1}{\delta\varphi_0} \end{bmatrix} \tag{3.6}$$

In Figure 3.7 below we plot the two Lyapunov exponents as well as their sum for two different electron entrance phases. For the case of isolated resonance the sum of Lyapunov exponents must be exactly zero. However for some of the electron entrance phases the Lyapunov exponents do not add up to zero.

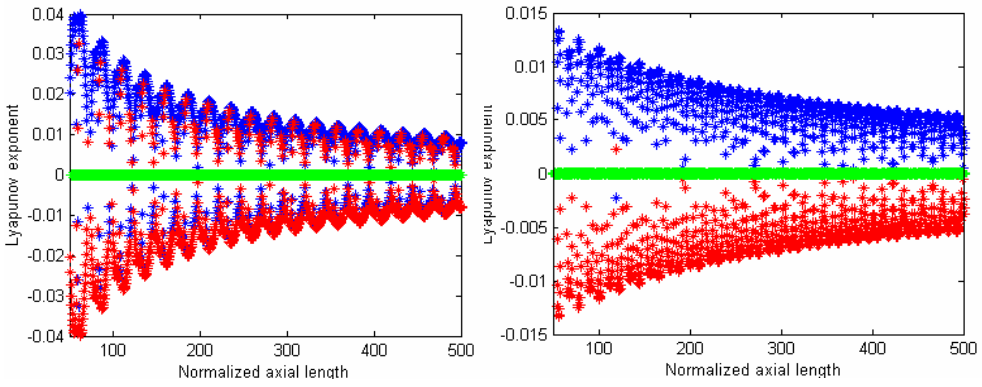

Figure 3.7: Lyapunov exponents plot for the case of isolated resonance and (a) $\gamma_0 = 1,\ \varphi_0 = \pi/4$ (b) $\gamma_0 = 1,\ \varphi_0 = 4\pi/5$.

Therefore, we fitted all the exponents in histograms as shown in Figure 3.8 and calculated the average at every axial length. One can observe from Figures 3.8 and

3.9 that as the normalized axial length $\xi \to \infty$ the average Lyapunov exponent slowly approaches zero.

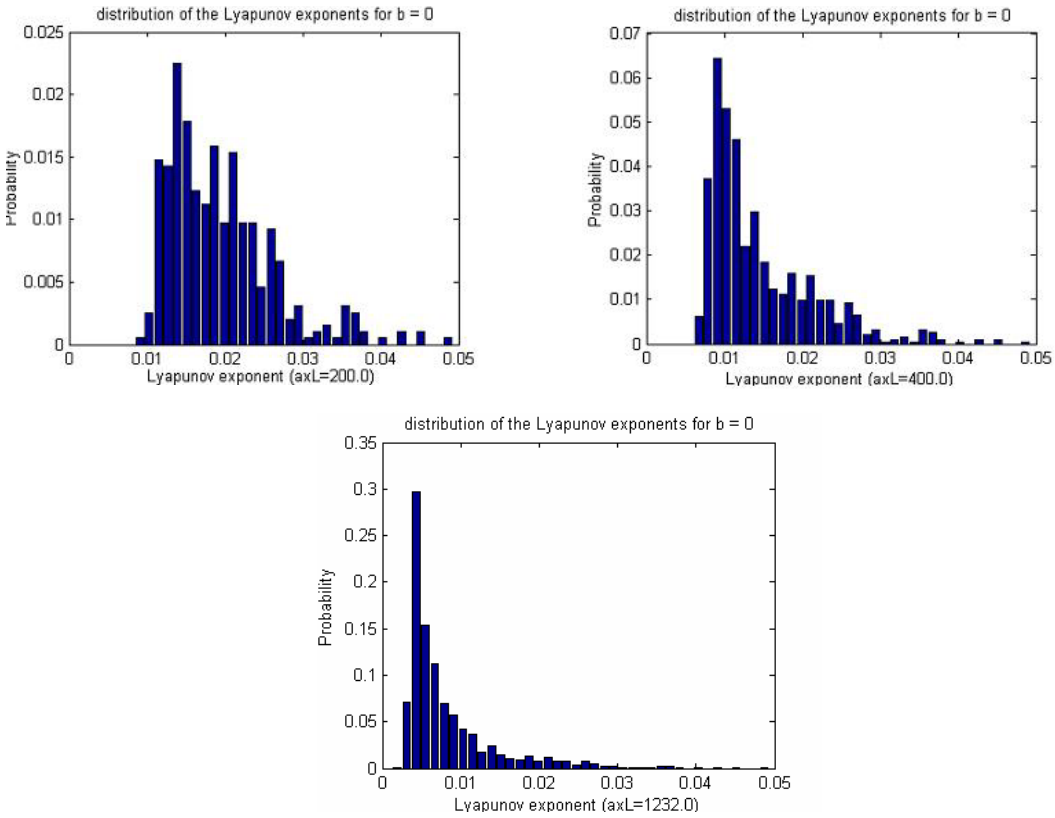

Figure 3.8: Histogram plots of Lyapunov exponents for isolated resonance case.

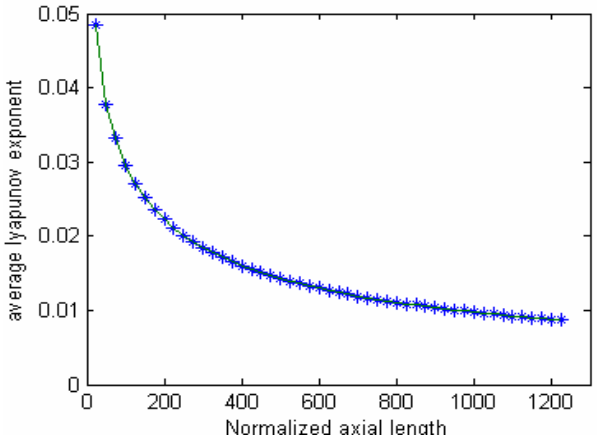

Figure 3.9: Average Lyapunov exponent plot.

3.5 Summary and conclusions

Two important results follow from the simulation results presented here:

(1) The overlapping of cyclotron resonances can cause electrons to exhibit stochastic motion.

(2) The overlapping of cyclotron resonances deteriorates the efficiency of the device.

The Lyapunov exponent method revealed that for the case of isolated resonance, one the electron trajectories can only be considered stationary for long realizations of the output waveguide. Therefore, for the case of overlapping of cyclotron resonances interaction the electron trajectories are indeed stochastic. It is important to mention that the normalized parameters considered here corresponded to those of a second harmonic relativistic gyrodevice driven by a 500kV electron beam and producing anywhere between 6 and 60MW output power [26].

Chapter 4: Wave Interaction in Relativistic Gyro-TWAs

4.1 Introduction

The interaction between waves in gyrodevices has been the focus of several publications looking to suppress or control undesired effects such as excitation of unwanted modes or mode competition [21-23, 29]. In these studies, emphasis has been on the controlling parasitic wave excitation in gyrotron oscillators. The few studies focused on gyro-traveling-wave amplifiers have been concerned by the suppression of backward wave excitation in these devices [29, 32]. Here we look at the interaction between forward waves in gyro-TWAs. If each of the electromagnetic waves has a different resonance condition with the electron beam, the overlapping of cyclotron resonances is possible [33].

In this Chapter we present numerical results for equations (2.122 - 124) and (2.127 - 128), which describe the interaction between three traveling symmetric $TE_{0,p}$ waves and the relativistic beam in the gyro-TWT and the gyrotwystron. Treatment for both devices differs only by the boundary conditions at the entrance to the output waveguide. While in the gyrotwystron the electron beam is pre-bunched prior to its insertion into the output waveguide, in the gyro-TWT the beam is launched into the waveguide in the same manner as in the TWT. In deriving these equations the following assumptions were made:

(1) The axial wavenumber of each wave was assumed to be $\pi / L \ll k_{sz} \ll \omega_s / c$ in order to ensure that only the forward wave ($\sim \exp(-ik_{sz} z)$) gets excited. We ignore parasitic backward wave excitation, which is usually a concern in gyro-TWAs [29].
(2) We assume that the wave amplitude $A(z,t)$ slowly varies of time and axial distance.
(3) We neglect drift in the guiding center (except that produced by the external magnetic field).
(4) We assume an ideal electron beam: no velocity or energy spread.

Below we first present simulation results for the case of isolated resonance in the gyro-TWT and gyrotwystron. Then, we present similar results for the case of overlapping of resonances. In both cases we consider an annular beam of radius 0.8cm, 500 kV, 400 A, and pitch factor $\alpha = 1$. The waveguide radius was 2.1cm and the RF driver frequency was 9 GHz. These values of the beam and waveguide parameters correspond to normalized beam currents $I_1 = 0.045$, $I_2 = 0.008$, $I_3 = 0.004$, and frequency mismatch parameters $\delta_1 = 0.132$, and $\delta_3 = -0.098$. The normalized axial wavenumbers of the three waves were $h_1 = 0.25$, $h_2 = 0.46$, and $h_2 = 0.51$, respectively. After presentation of the results an analysis follows, then the Chapter is summarized.

4.2 Simulation results for the case of isolated resonance

4.2.1 Gyro-TWT

For this case of isolated resonance (*b = 0*), the wave excitation and electron motion equations reduce to

$$\frac{dF_1}{d\xi} = -\frac{I_1}{2\pi} e^{-i\delta_1 \xi} \int_0^{2\pi} \frac{p_\perp}{2} e^{-i\varphi} d\varphi_0 \,,$$

$$\frac{dF_2}{d\xi} = -\frac{I_2}{2\pi} \int_0^{2\pi} \frac{p_\perp^2}{2} e^{-i2\varphi} d\varphi_0 \,, \qquad (4.1)$$

$$\frac{dF_3}{d\xi} = -\frac{I_3}{2\pi} e^{-i\delta_3 \xi} \int_0^{2\pi} \frac{9 p_\perp^3}{16} e^{-i3\varphi} d\varphi_0 \,,$$

$$\frac{d\gamma}{d\xi} = \frac{p_\perp}{2} \Re e \left\{ F_1 e^{i(\varphi + \delta_1 \xi)} + p_\perp F_2 e^{i2\varphi} + \frac{9}{8} p_\perp^2 F_3 e^{i(3\varphi + \delta_3 \xi)} \right\} \qquad (4.2)$$

$$\frac{d\varphi}{d\xi} = \gamma - 1 + \Delta - \Re e \left\{ iF_1 e^{i(\varphi+\delta_1\xi)} \left(1 - \frac{\gamma}{p_\perp^2}\right) \frac{p_\perp}{2} + + iF_2 e^{i2\varphi} \left(1 - \frac{\gamma}{p_\perp^2}\right) \frac{p_\perp^2}{2} + iF_3 e^{i(3\varphi+\delta_3\xi)} \left(1 - \frac{\gamma}{p_\perp^2}\right) \frac{9 p_\perp^3}{16} \right\}$$

The boundary conditions at the entrance of the waveguide are:

$$\gamma(0) = 1 \,, \quad \varphi(0) = \omega_s t_0 - \theta_0 = \varphi_0 \in [0, 2\pi) \,, \quad p_\perp(0) = \beta_{\perp_0} \qquad (4.3)$$

First, the magnetic field was optimized for achieving the most efficient interaction between the beam and the TE_{01} wave. That is the parameter Δ was tuned so that the RF driver initially excited the TE01 wave only. The results are shown in Figures 4.1 - 4.4 for the initial normalized field amplitudes $F_1(0) = 0.005$, $F_2(0) = 0$, $F_3(0) = 0$, and the initial cyclotron resonance detuning $\Delta = 0$ (recall that $\Delta = 1 - h_2 \beta_{z_0} - \mu$). In Figure 4.1 the normalized wave intensities are shown as functions of the axial distance. One can see that the high frequency waves (TE_{02} and TE_{03}) experience a significant growth. The excitation of the TE_{02} and TE_{03} waves is a typical case of generation of signal frequency harmonics common in TWT's [4]: the resonance interaction between the TE_{01} wave and the electron beam gives rise to

harmonics of the signal frequency in the current density term, which in turn excites the high order modes. The gain of the TE_{01} wave is shown in Figure 4.2. This curve does not depend on the other waves because the second and third waves absorb only a small amount of energy from the beam. Figure 4.3 shows the electron phases as a function of the normalized axial waveguide distance. Figure 4.4 shows the position of electrons in the phase space ($p_x = p_\perp \cos\varphi$ and $p_y = p_\perp \sin\varphi$) at the entrance to the waveguide and at the point of maximum efficiency. From the last two figures it is apparent that the TE_{01} wave is dominant because a single electron bunch is formed.

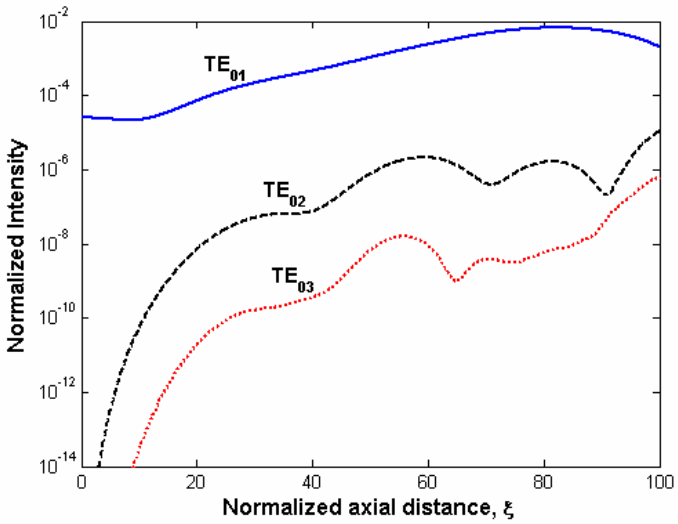

Figure 4.1: Axial dependence of wave intensities in the fundamental harmonic gyro-TWT for $b = \Delta = 0$.

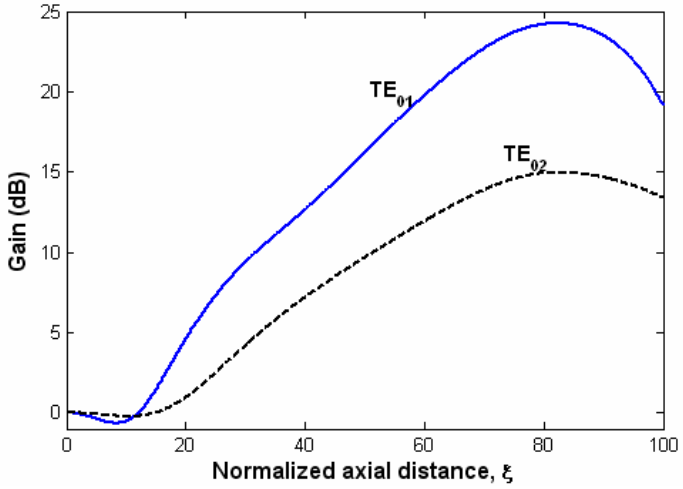

Figure 4.2: Gain of the gyro-TWT in the absence of resonances overlap ($b = 0$).

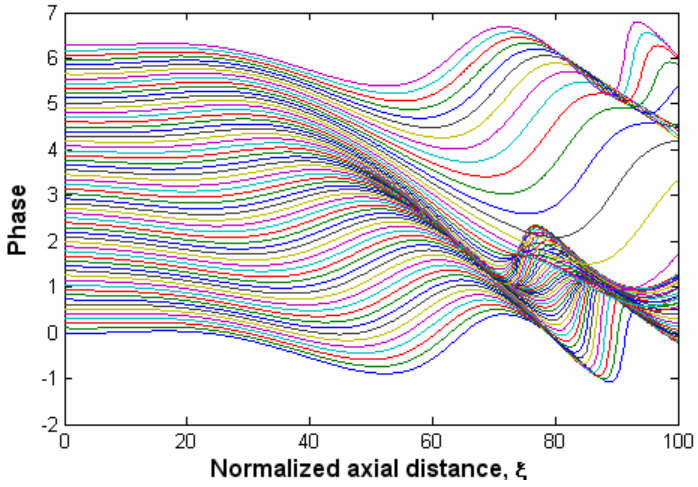

Figure 4.3: Electron phases in the fundamental harmonic gyro-TWT for $b = \Delta = 0$.

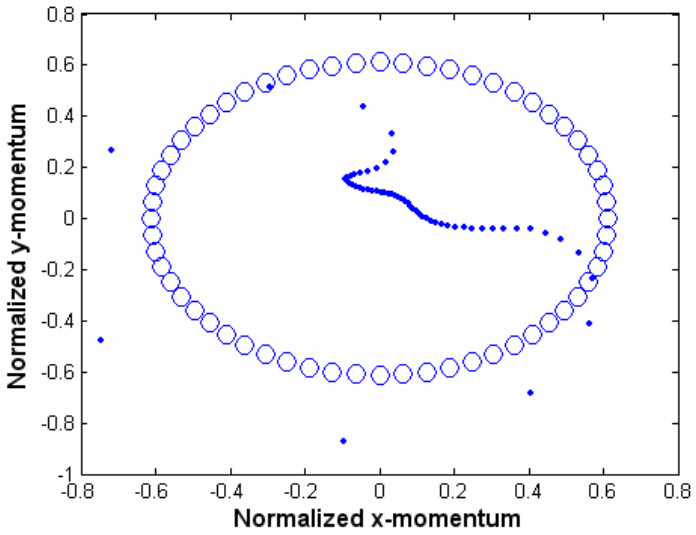

Figure 4.4: Electron locations in the phase space ($p_x = p_\perp \cos\varphi$, $p_y = p_\perp \sin\varphi$) of the gyro-TWT for $b = \Delta = 0$ at the waveguide entrance ($\xi = 0$ - circles) and at $\xi = 80$ (dots) where the gain and efficiency are maximal.

Next, the parameter Δ was tuned so that the electron beam interacted primarily with the TE_{02} wave at the second cyclotron harmonic. The axial dependence of the intensities of all three waves is shown in Figure 4.5 for initial normalized field amplitudes $F_1(0) = 0.0001$, $F_2(0) = 0.005$, $F_3(0) = 0.0001$, and initial cyclotron resonance detuning $\Delta = 0.046$. The normalized intensities of the two waves TE_{01} and TE_{03} can be seen increasing with the axial length, but they remain significantly smaller than the primary wave intensity. The excitation of the neighboring harmonics due to the excitation of the second harmonic wave is a typical nonlinear process known as 'four-photon decay process' [21]. The gain curve presented in Figure 4.2 (dashed line) shows no significant change when calculated for the case of parametric excitation (i.e., when all three waves are excited). However the maximum gain is smaller than the value obtained for the fundamental harmonic operation. The phase

plot and the electron trajectories presented in Figures 4.6 and 4.7 show two electron bunches separated by an angular distance of π. This confirms that the second harmonic TE_{02} wave is the dominant mode in this interaction, because the formation of two electron bunches corresponds to the quadrupole nature of the second harmonic resonance field.

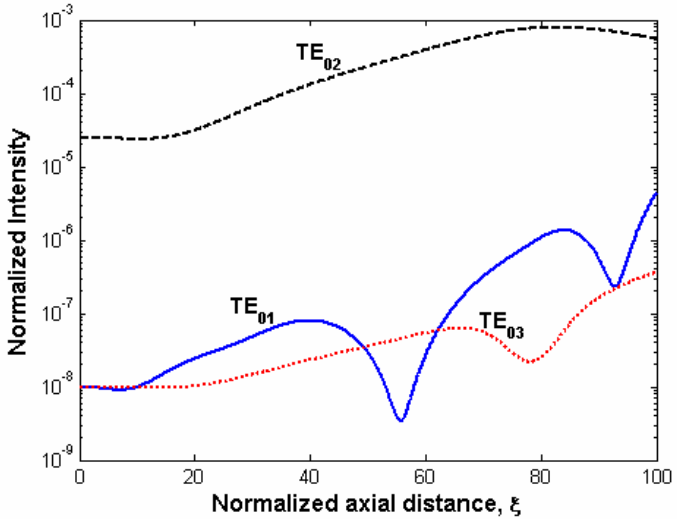

Figure 4.5: Axial dependence of wave intensities in the second harmonic gyro-TWT for b = 0 and $\Delta = 0.046$.

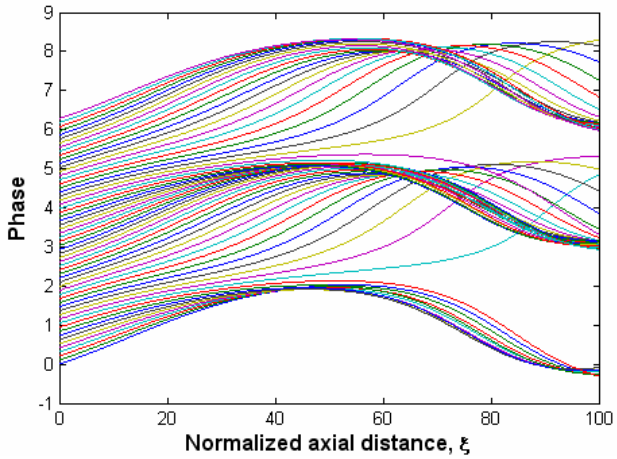

Figure 4.6: Electron phases in the second harmonic gyro-TWT for b = 0 and $\Delta = 0.046$.

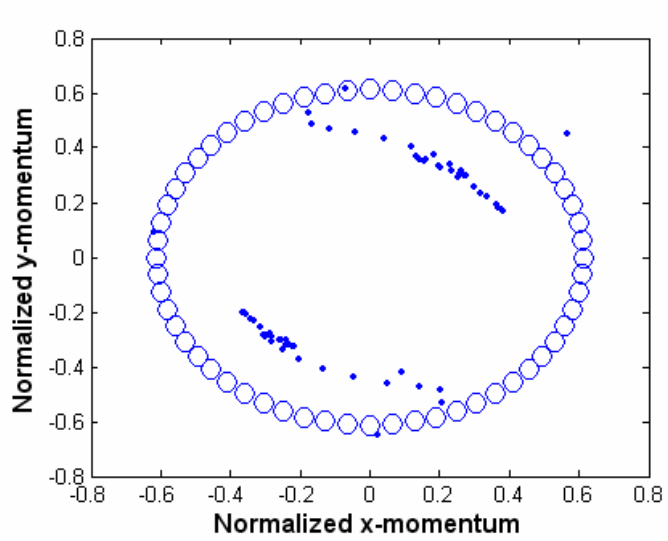

Figure 4.7: Electron locations in the phase space ($p_x = p_\perp \cos\varphi$, $p_y = p_\perp \sin\varphi$) of the gyro-TWT at the waveguide entrance ($\xi = 0$ - circles) and at $\xi = 80$ (dots) for $b = 0$ and $\Delta = 0.046$.

4.2.2 Gyrotwystron

Equations 4.1 and 4.2 were solved with the following boundary conditions:

$$\gamma(0) = 1, \quad \varphi(0) = \varphi_0 + q\sin\varphi_0, \quad \varphi_0 \in [0, 2\pi), \quad \text{and} \quad F(\xi = 0) = 0, \tag{4.4}$$

First, the magnetic field was optimized so as to achieve the most efficient interaction between the modulated electron beam and the TE_{01} wave. The simulation results are shown in Figures 4.8 - 4.10 for bunching parameter $q = 1.5$ and the detuning parameter $\Delta = -0.03$. The axial dependence of the three normalized wave intensities are shown in Figure 4.8. There, the normalized intensity of each wave is shown for two cases: when the beam interacts with a single wave (solid lines) and when the beam interacts with a wave in presence of other waves (dashed lines). It is apparent

that the radiation intensity of each wave decreases slightly when the wave interacts with the beam in the presence of other waves (parametric interaction). This can be explained by the fact that each wave extracts some energy from the same beam. The net efficiency of the device is shown in Figure 4.9 along with the efficiency curves for the case of single wave interaction. It is clear that the net efficiency of the device is a little higher than the efficiency obtained when only the dominant mode (TE_{01}) interacts with the beam. Therefore, the nonlinear excitation of the side modes can slightly improve the net efficiency of the device in this case. In Figure 4.10 the electrons are shown at the entrance of the waveguide and at $\xi = 34$ where the efficiency is maximum.

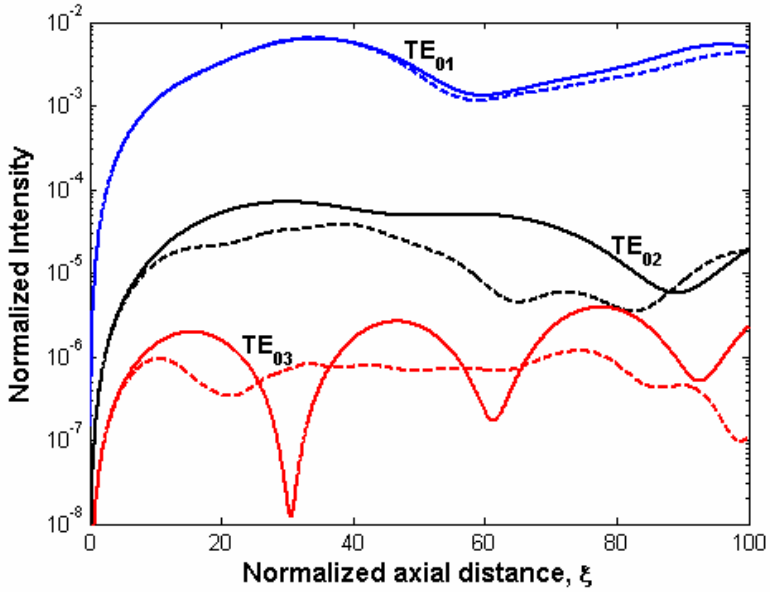

Figure 4.8: Axial dependence of wave intensities in the gyrotwystron for the case of single wave interaction (solid lines) and for the case of parametric wave excitation (dashed lines) when b = 0 and $\Delta = -0.03$.

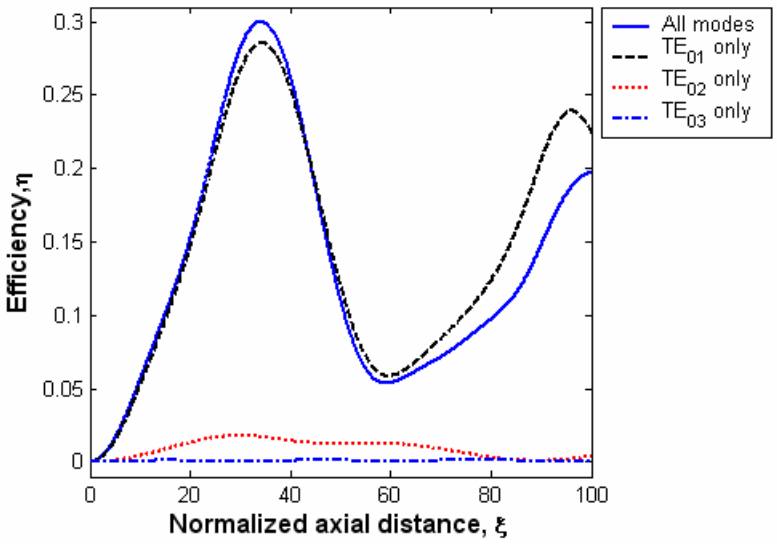

Figure 4.9: Efficiency of the gyrotwystron for parametric interaction and single wave excitation interaction when b = 0 and $\Delta = -0.03$.

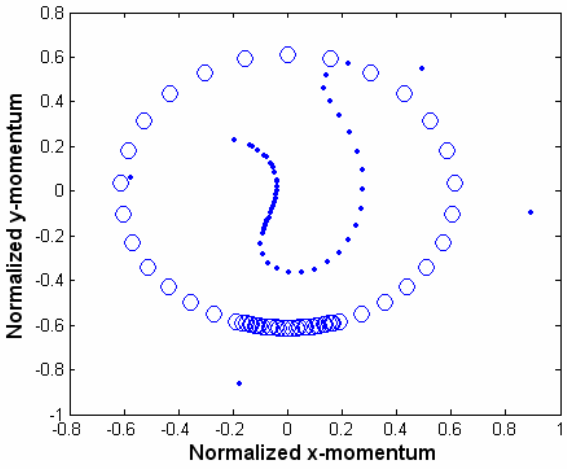

Figure 4.10: Electron positions in the phase space ($p_x = p_\perp \cos\varphi$, $p_y = p_\perp \sin\varphi$) of the gyrotwystron with $b = 0$, $\Delta = -0.03$ at the waveguide entrance ($\xi = 0$ - circles) and at $\xi = 34$ (dots) where the efficiency is maximal.

4.3 Simulation results for the case of overlapping resonances

4.3.1 Gyro-TWT

In this case Eqs 2.122-124 and 2.127-128 were simulated for the same scenarios discussed in Section 4.2.1, viz., the dominant TE_{01} and the dominant TE_{02} waves. Figure 2.11 presents the normalized wave intensities for the dominant TE_{01}. For easy comparison the intensities are plotted for the non-overlapping (b = 0 - solid lines), and overlapping cyclotron resonances (b = 0.5 - dashed lines) cases. One can note that while the maximum intensity of each of the waves remains essentially the same, the overlapping of resonances causes significant rippling in the intensity curves of the TE_{02} and TE_{03} waves. In Figure 2.12 similar results are shown for the case when the magnetic field is tuned so as to excite primarily the TE_{02} wave. It appears from these curves that the overlapping of resonances increases the intensity of the TE_{01} and TE_{03} waves significantly. The maximum gain for the case of resonance overlap is the same as the value obtained in the absence of resonances overlap. The curves are similar to those shown in Figure 4.2 with the exception that for b = 0.5 a significant amount of rippling appears.

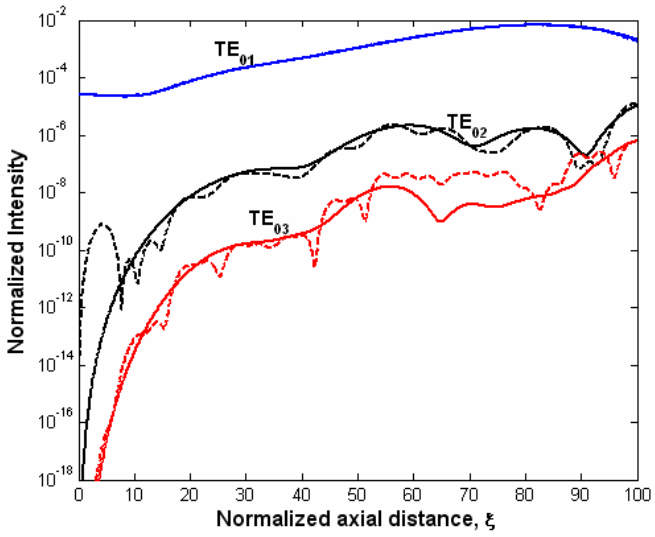

Figure 4.11: Axial dependence of wave intensities in the fundamental harmonic gyro-TWT for b = 0 (solid lines) and b = 0.5 (dashed lines) when $\Delta = 0$.

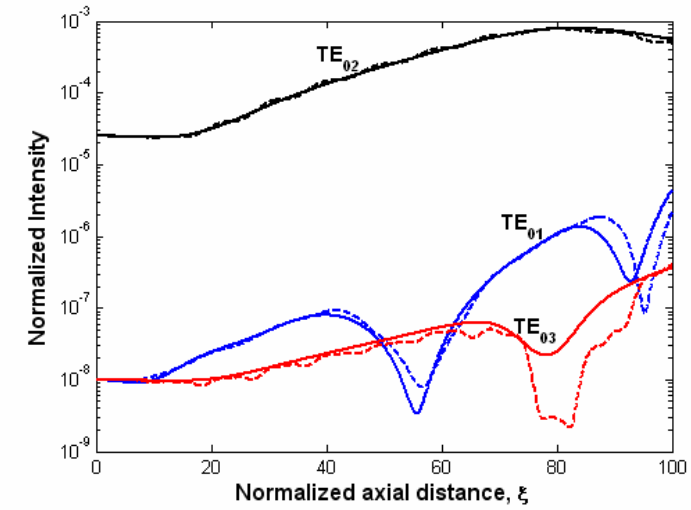

Figure 4.12: Axial dependence of wave intensities in the second harmonic gyro-TWT for b = 0 (solid lines) and b = 0.5 (dashed lines) when $\Delta = 0.046$

4.3.2 Gyrotwystron

Simulation results are presented for the same initial condition given in Section 4.2.2 with b = 0.5. In Figure 4.13, the normalized wave intensities are shown for the case of single harmonic interaction of the electron beam and waves (solid lines), and for the overlapping of resonances case (dashed lines). The efficiency curves are plotted for both cases in Figure 4.14. From these figures it is apparent that while the overlapping of cyclotron resonances does not cause significant changes in the net efficiency of the device, it causes significant rippling in the intensity curves.

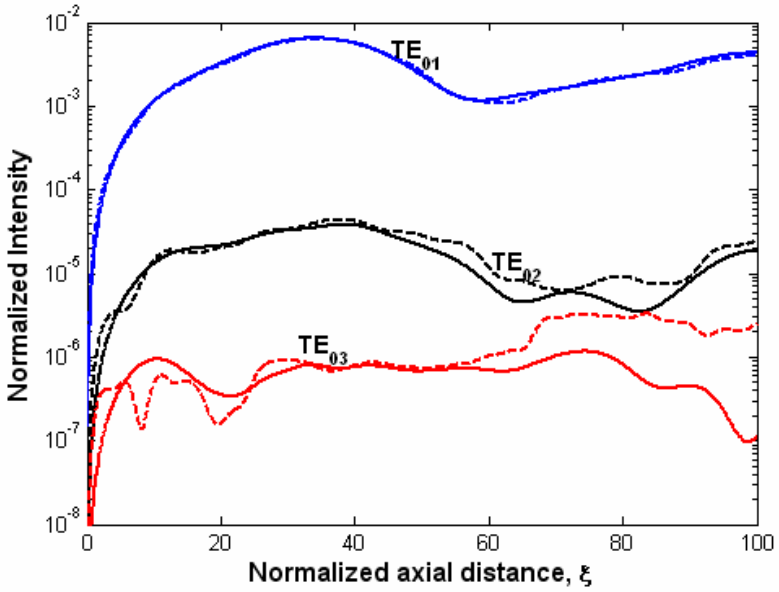

Figure 4.13: Axial dependence of wave intensities in the gyrotwystron for b = 0 (solid lines) and b = 0.5 (dashed lines) when $\Delta = -0.03$.

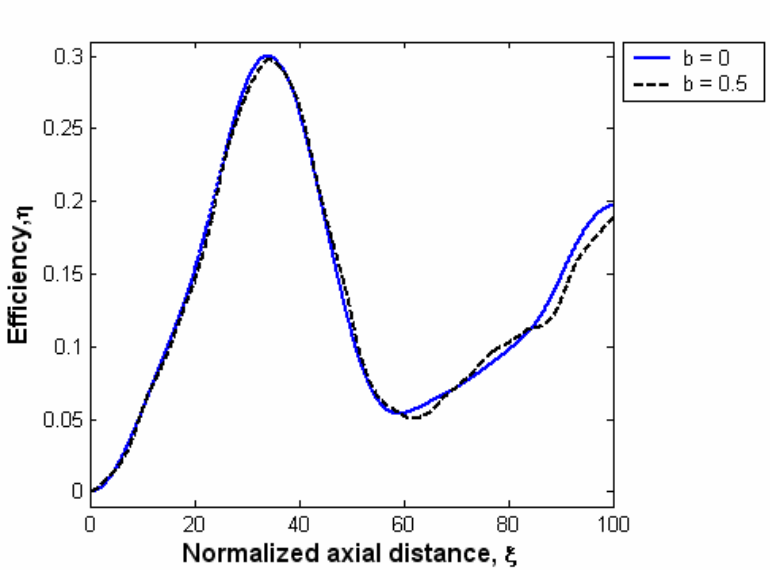

Figure 4.14: Axial dependence of gyrotwystron efficiency for b = 0 (solid lines) and b = 0.5 (dashed lines) when $\Delta = -0.03$.

4.4 Analysis of simulation results

From the numerical results above it appears easier to excite high frequency waves when operating at low frequency mode in the gyro-TWT. In the case of operation at the second harmonic, for example, the excitation of the first and third waves could not start from noise level, i.e., with $F_1(0) = F_3(0) = 0$. Therefore, simulations were done with a small, but non-zero value of $F_{1,3}(0)$. One can also observe that the "parasitic" waves do not present too much of a competition to the dominant wave in terms of the power absorbed from the beam in both gyro-TWA configurations. The highest radiation intensity from these side waves is about 40dB below the intensity of the primary wave. Another interesting observation, which can be made from the results, is that the maximum intensity of a given wave does not vary much whether this wave is excited alone or in the presence of other waves

(parametric excitation). One can note that the overlapping of cyclotron resonances does not affect the maximum wave intensities either. However it results to significant rippling in the curves. This may be an indication of stochasticity in the wave interaction process, as discussed in [33]. The nonlinear excitation of additional waves due to the parametric interaction appears to affect the gyrotwystron performance more than the gyro-TWT performance, certainly, because the waves have comparable initial amplitude values in the former.

In the numerical analysis presented above the relativistic beam characteristics were similar to those of the beam used in the relativistic gyrotwystron experiments at the University of Maryland [17, 34]. The relatively high efficiency obtained here (30% compare to 21%) can be explained by the fact that we considered a cold beam in our simulations. The initial normalized field amplitude of the excited wave, $F(0) = 0.005$, corresponds to an input power of about 56.8 kW for the fundamental cyclotron harmonic resonance operation and 81.4 kW for the case of second harmonic resonance operation. These approximate values were obtained through the use of the following relation [35]:

$$F(0) = 0.96 \times 10^{-3} \kappa^2 \sqrt{G_{cpl} P_{in}(kW)/h}\,. \tag{4.5}$$

Here, G_{cpl} is the coupling coefficient for an annular beam of radius R_0 interacting with the $TE_{m,p}$ mode of a circular waveguide given by

$$G_{cpl} = \frac{J^2_{m\mp s}(k_\perp R_0)}{(\nu^2 - m^2) J^2_m(\nu)}\,. \tag{4.6}$$

These input power values are within the experimental range of values [35, 36].

4.5 Summary and conclusions

This Chapter addressed the interaction between three waves at different harmonics of the electron cyclotron frequency. It was shown that when an electron beam excites one of the waves, two other waves could be excited nonlinearly. It was also shown that the overlapping of cyclotron resonances does not affect the output power level. However it causes significant oscillations in the output radiation and gain curves. Varying the frequency signal mismatch δ in the simulations could help determine if these oscillations are due to traces of stochasticity in the interaction. But this was not the focus of the study. The beam parameters used in the simulations were similar to those of a relativistic gyro-amplifier. The maximum efficiency was achieved for a waveguide length of 26cm in the gyro-TWT and 11cm in the gyrotwystron with a 9 GHz RF driver. These waveguide length values may give rise to the excitation of parasitic backward waves, which were not taken into account in our analysis.

Chapter 5: Conclusion

This thesis investigated two nonlinear dynamic processes in relativistic gyro-traveling wave amplifiers: (1) the effect of the overlapping of cyclotron resonances on electron trajectories and (2) the interaction between waves both in the absence of the overlapping of cyclotron resonances and when it is present. Relativistic gyro-TWAs were considered because they are being developed to drive advanced radars and future linear colliders, which are both high power applications at millimeter wavelengths. The presence of any important stochastic effect in the beam wave dynamic can adversely affect the performance of the device. Another motivation for the choice of gyro-amplifiers is that most nonlinear studies have focused solely on gyrotron oscillators.

Nonlinear equations were derived following the known gyro-TWT theory for a relativistic beam interacting primarily with a forward propagating wave at the first three cyclotron harmonics. Numerical simulations of these equations for the case of a large constant amplitude wave showed that electron trajectories could be chaotic when the overlapping of cyclotron resonances occurs. Using the Lyapunov exponent method we showed that electron trajectories are more or less stationary in the case of isolated resonance. It revealed that the average Lyapunov exponent approaches zero for an infinitely long waveguide.

The nonlinear equations describing the single wave interaction with the electron beam were expanded to include three symmetric $TE_{0,p}$ -waves resonant with the beam at three different cyclotron harmonics. Numerical simulations of these

equations assuming a relativistic beam and a signal frequency of 9 GHz showed that both “three photon” and “four-photon” nonlinear processes can take place. When the overlapping of resonances was included significant rippling was noted in the radiation curves. Future possible work here include finding the correlation between electron stochastic motion and the rippling in the radiation curve in order to determine the onset of chaos in the system.

Bibliography

[1] H. Hertz, *.Electric waves*, Dover Publications, New York 1962.

[2] E. Okress, Ed., *Cross-Field Microwave Devices*, Academic Press, New York, 1961.

[3] R. J. Baker, J. H. Broske, N. C. Luhman, Jr., G. S. Nusinovich, Eds. *Modern Microwave and Millimeter wave Power Electronics*, IEEE Press, Piscataway, 2004.

[4] A. S. Gilmour, Jr., *Microwave Tubes,* Artech House, Norwood, 1981.

[5] M. Radmanesh, *Radio Frequency Microwave Electronics,* Prentice Hall, 2001.

[6] K. L. Felch, B. G. Danly, H. R. Jory, K. E. Kreischer, W. Lawson, B. Levush and R. J. Temkin, "Characteristics and Applications of Fast-Wave Gyrodevices", *Proc. of the IEEE*, **87**, (1999).

[7] R. J. Barker, E. Schamiloglu, Eds., *High-Power Microwave Sources and Technologies*, IEEE Press, New York, 2001.

[8] G. S. Nusinovich, *Introduction to the Physics of Gyrotrons*, The Johns Hopkins University Press, Baltimore, 2004.

[9] S. H. Gold and G. S. Nusinovich, "Review of high-power microwave source research", *Rev. Sci. instrum*., **68**, 3945, (1997).

[10] A. V. Gaponov-Grekhov and V. L. Granatstein, Eds. *Application of High-Power Microwaves*, Artech House, Boston, 1994.

[11] A. Grudiev, *Numerical Study of Nonstationary Phenomena in Gyro-Oscillators,* Cuvillier Verlag, Gottingen, 2003.

[12] K. R. Chu, "The electron cyclotron maser", *Rev. Modern Phys*., **76**, 489, (2004).

[13] P. A. Sturrock, "Kinematics of Growing Waves", *Phys. Rev*., **112**, 1488 (1958).

[14] P. Sprangle and A. T. Drobot, "The Linear and Self- Consistent Nonlinear Theory of the Electron Cyclotron Maser Instability", *IEEE Trans. Microwave Theory and Tech*., **25**, 528, (1977).

[15] V. A. Flyagin, A. V. Gaponov, M. I. Petelin and V. K. Yulpatov, "The Gyrotron", *IEEE Trans. Microwave Theory and Tech.*, **25**, 514, (1977).

[16] G. S. Nusinovich, P.E. Latham, and O. Dumbrajs, "Theory of relativistic cyclotron masers", *Phys. Rev. E*, **52**, 998 (1995).

[17] W. Lawson, P. E. Latham, J. P. Calame, J. Cheng, B. Hogan, G. S. Nusinovich, V. Irwin, V. L. Granatstein and M. Reiser, "High power operation of first and second harmonic gyrotwystrons", *J. Appl. Phys.* **78**, 550, (1995).

[18] P. A. Lindsay and X. Chen, "Chaos and Gyrotron Type of Interaction", *IEEE Trans. Plasma Sci.*, **22**, 834 (1994).

[19] O. Dumbrajs, R. Meyer-Spasche, and A. Reinsfelds, "Analysis of Electron Trajectories in a Gyrotron Resonator", *IEEE Trans. Plasma Sci.*, **26**, 847 (1998).

[20] J. C. Rodgers, T. M. Antonsen, Jr., and V. L. Granatstein, "Harmonic Gain and Noise in a Frequency-Doubling Gyro-Amplifier", *IEEE Trans. Elect. Dev*. **50**, 1785 (2003).

[21] G. S. Nusinovich, "Mode interaction in gyrotrons", Int. J. Electron., **51**, 457, (1981).

[22] G. S. Nusinovich, "Parametric instabilities in gyro-devices at cyclotron harmonics", *Int. J. Electron*., **72**, 795, (1992).

[23] G. P. Saraph, T. M. Antonsen, Jr., G. S. Nusinovich and B. Levush, "A study of parametric instability in a harmonic gyrotron: Designs of third harmonic gyrotrons at 94 GHz and 210 GHz", *Phys. Plasmas*, **2**, 2839, (1995).

[24] A. V. Yulpatov, "Nonlinear theory of the interaction between a periodic electron beam and an electromagnetic wave," *Radiophysics and Quantum Electronics*, **10** 471, (1967)"

[25] G. S. Nusinovich, and H. Li, "Theory of gyro-travelling-wave tubes at cyclotron harmonics", *Int. J. Electron*., **72**, 895, (1992); "Theory of the relativistic gyrotwistron", *Phys. Fluids B*, **4**, 1058 (1992).

[26] G. S. Nusinovich, R. Ngogang, T. M. Antonsen, Jr. and V. L. Granatstein, "Overlapping of Resonances and Stochasticity of Electron Trajectories in Cyclotron Masers", *Phys. Rev. Lett.*, **93**, 055101, (2004).

[27] D. M. Pozar, *Microwave Engineering* , John Wiley & Sons,. New York 1998.

[28] J. Sirigiri, "Theory and design study of a novel quasi-optical gyrotron traveling wave amplifier", Master's thesis, Massachusetts Institute of Technology, Department of Electrical Engineering and Computer Science, October 1999.

[29] G. S. Nusinovich, "Review of the Theory of Mode Interaction in Gyrodevices"

IEEE Trans. Plasma Sci.. **27**, 313 (1999).

[30] A. J. Lichtenberg and M. A. Lieberman, *Regular and Chaotic Dynamics*, Springer-Verlag, New York, 1992.

[31] E. Ott, *Chaos in Dynamical Systems*, Cambridge University Press, Cambridge, 2002.

[32] P. E. Latham and G. S. Nusinovich, "Theory of relativistic gyro-traveling wave devices", *Phys. Plasmas*, **2**, 3494 (1995).

[33] V. A. Buts, O. V. Manuilenko, K. N. Stepanov, and A. P. Tolstoluzhskii, "Chaotic Charged Particle Dynamics in Wave-Particle Interaction. Chaotic Wave Dynamics in Weak Nonlinear Wave –Wave Interaction", *Plasma Phys. Rep.*, **20**, 714 (1994).

[34] V.L. Granatstein, and W. Lawson, "Gyro-Amplifiers as Candidate RF Drivers for TeV Linear Colliders", *IEEE Trans. Plasma Sci.* **24,** 648, (1996).

[35] G. S. Nusinovich, and M. Walter, "Theory of the inverted gyrotwystron", *Phys. Plasmas* **4**, 3394 (1997).

[36] R. Ngogang, G. S. Nusinovich, T. M. Antonsen, Jr. and V. L. Granatstein, "Wave interaction in relativistic harmonics gyro-traveling wave devices" *Phys. Rev.E.*, **(**publication pending).